JGR Space Physics

RESEARCH ARTICLE
10.1029/2022JA030615

Key Points:

- Energy conversion is always present in the equatorial region near to or overlapping with places where there is ultra-low frequency (ULF) wave intensification
- Energy conversion occurs predominantly between magnetic and internal energies with a smaller contribution of the kinetic energy term
- Higher dynamic pressure significantly increases energy conversion rate and ULF wave activity in both dayside and nightside magnetosphere

Correspondence to:
P. R. Jauer,
pauloricardojauer@gmail.com

Citation:
Jauer, P. R., Wang, C., Echer, E., Souza, V. M., Da Silva, L. A., Marchezi, J. P., et al. (2022). Global modeling of the inner magnetosphere under the influence of a magnetic cloud associated with an interplanetary coronal mass ejection: Energy conversion and ultra-low frequency wave activity. *Journal of Geophysical Research: Space Physics*, *127*, e2022JA030615. https://doi.org/10.1029/2022JA030615

Received 4 MAY 2022
Accepted 30 SEP 2022

Global Modeling of the Inner Magnetosphere Under the Influence of a Magnetic Cloud Associated With an Interplanetary Coronal Mass Ejection: Energy Conversion and Ultra-Low Frequency Wave Activity

P. R. Jauer[1,2], C. Wang[2], E. Echer[1], V. M. Souza[1], L. A. Da Silva[1,2], J. P. Marchezi[1,2], L. R. Alves[1], M. V. Alves[1], S. Douglas[1,2], C. Loesch[3], Z. Liu[2], L. Hui[2], L. E. A. Vieira[1], W. D. Gonzalez[1], C. M. Denardini[1], C. Medeiros[1], and J. E. R. Costa[1]

[1]National Institute for Space Research—INPE, São José dos Campos, Brazil, [2]State Key Laboratory of Space Weather, National Space Science Center, Chinese Academy of Sciences, Beijing, China, [3]Institute of Higher Education of Brasília—IESB: Centro Universitário, Brasília, Brazil

Abstract The interaction and response of the magnetic cloud-type structure with Earth's magnetosphere were modeled by the SWMF/BATS-R-US code. The conversion of magnetic (E_m), kinetic (E_k), and internal (E_i) energies was analyzed as well as the wave power integrated in the ultra-low frequency (ULF) range of the poloidal (E_ϕ) and toroidal (E_r) electric field components in the equatorial region of the magnetosphere, in seven 2-hr long intervals, namely, *I*1 through *I*7. The intensity of energy conversion and wave activity for *I*1 and *I*7 intervals was negligible. The energy conversion started in the *I*2 interval and extended to the *I*3, *I*4, and *I*5 intervals. The power of the E_ϕ and E_r components in the dayside and nightside regions is clearly observed. The *I*4 corresponds to interplanetary magnetic field (IMF) B_z mostly southward and the *I*5 has similar amplitudes of the B_z and B_y components, corresponding to the period of the high geomagnetic activity. The conversion rate for the *I*4 and *I*5 was similar, however, the integrated power spectral density (IPSD) of the E_ϕ and E_r components is more intense in *I*5. During the *I*6 interval, with predominant IMF B_y, the energy conversion rate is intensified mostly for inner radial distances $R < 6\ R_E$, and the E_k component becomes close to zero for outer regions. The energy conversion regions are located spatially close to or overlapping with regions where the IPSD in the ULF range is intensified. The energy conversion in the inner magnetosphere occurred preferentially between E_m and E_i, with the E_k energy component always present but with lower intensities.

1. Introduction

The Sun continually emits mass, momentum, and energy in the form of magnetized and ionized plasma from its outermost layer known as the solar wind (Hundhausen, 2012). The variation in energy content is closely related to the solar cycle. During the minimum activity phase, the predominant solar structures are the coronal holes (CH), from where the fast solar wind streams continuously emanate (Schwenn, 2006; Gosling, 1997; Gosling et al., 1976, and references therein). The interaction of ambient solar wind and fast solar wind forms the regions known as co-rotating interaction regions or CIR's (Alves et al., 2006; Smith & Wolfe, 1976). During the maximum solar activity phase, the predominant large-scale solar structures are the sunspots and active regions, where continuous magnetic reconfigurations release a large amount of magnetized plasma into the interplanetary space known as Coronal Mass Ejections (CME). A subclass of CMEs identified in the interplanetary medium is the magnetic clouds (MC) (Burlaga & Burlaga, 1995; Burlaga et al., 1998) An important characteristic of MC concerns its signature observed by the satellite when crossing the flux tube magnetic structure, which can be seen as an intense magnetic field with smooth rotation and low plasma beta value, also being able to be defined as a force-free structure having cylindrical symmetry (see, Kilpua et al., 2017; Goldstein, 1983, for more details). These MC-type solar and interplanetary structures in comparison to structures that are predominant in the minimum of solar activity can intensely and abruptly affect the magnetosphere-ionosphere system and upper atmosphere if they have a southward-directed interplanetary magnetic field (IMF) component through magnetic reconnection (Dungey, 1961). The primary evidence of the abrupt penetration of mass, momentum, energy, and magnetic flux into the inner regions of the magnetosphere is the emergence of magnetic storms and substorms (Chapman & Ferraro, 1933; Gonzalez et al., 1994), together with global perturbations in the particle flux which make up the ring current (RC) and the Radiation Belts (RB) that are highly influenced by the occurrence of

wave-particle interactions which in turn engender both acceleration and loss processes (Baker, 2021; Baker et al., 2004; Zong, 2022).

Many studies in the last decades, through observation and numerical simulations, are providing important information on the coupling of geoeffective interplanetary structures and the possible causes of the variation of energetic particle populations in the magnetospheric environment, (see, e.g., Baker, 2021; Baker et al., 2004; Claudepierre et al., 2008, 2010; Da Silva et al., 2019; Ebihara et al., 2005; Elkington, 2006; Fok et al., 2014; Jauer et al., 2019; Souza et al., 2018; Paral et al., 2015, and references therein). The magnetosphere can be considered as an electromagnetic resonance box where many wave propagation modes can coexist and interact with preexisting particle populations accelerating them to relativistic levels. Through numerical experiments, Claudepierre et al. (2010) showed that pressure pulses existing in the solar wind have the ability to generate disturbances in the poloidal and toroidal electric field components in the ultra-low frequency (ULF) PC5 range. This modulation of ULF waves can be effective in accelerating electrons in the region of the outer radiation belts and cause radial diffusion (Elkington, 2006; Elkington et al., 1999) either due to oscillations in the electric and magnetic fields in the inner magnetosphere (IM) caused by the interaction of interplanetary structures with Earth's magnetosphere or due to internal processes associated with magnetospheric convection. Baker and Daglis (2007) showed a great variability of the 2–6 MeV energy range electron flux in the outer radiation belt measured by (SAMPEX, Solar Anomalous, and Magnetospheric Particle Explorer) around the minimum phase of solar activity in 1994 and around the maximum of solar activity in 2003. During the minimum, the variability of the electron flux is modulated by interplanetary structures that cause recurrent HSS/CIR's-related magnetic storms. During the period of maximum solar activity, the predominant solar transient structures are the active regions where solar flares and CMEs can occur. In this period the interplanetary medium and the global magnetosphere (GM) are subject to an intense coupling due to the characteristics of magnetic field and velocity. From October–November 2003, the IM experienced a strong and singular response due to the interaction of a set of CMEs there was a substantial increase in energy level and electron flux that extended from the slot region $L \sim 2.0$ to near the geosynchronous orbit $L \sim 6.6$ (Baker et al., 2004). Several effects on the technological system, and on the ground, have been studied and reported. Device failures aboard satellites such as power supply and degradation, and auroral brightness was seen at low latitudes were also reported (Lopez et al., 2004). 29–31 October 2003, was an intense period of coupling of a CME-type interplanetary structure with the Earth's magnetosphere, promoting an intense period of energy transfer and conversion in the global, inner, and ground magnetosphere. Large and intense Geomagnetically induced currents (GIC) were intensified due to the emergence of a super geomagnetic storm, which was responsible for an hour-long blackout in southern Sweden (Pulkkinen et al., 2005).

In this way, we can see that the interaction between solar structures can be the trigger of an abrupt transfer and conversion of energy in the environment of the global and IM and the study of this coupling is of paramount relevance from a scientific, technological and human point of view. Today humanity reaches a high dependence on technological systems that are affected by solar activity. Looking at our past Carrington-type events (Carrington, 1859) would have unprecedented impacts on the magnetospheric environment. Thus, it is of great importance to understand the mechanisms of the coupling of CME-type events that cause abrupt energy conversion and also the amplification and propagation of perturbations that cause the interaction with particles that surround the Earth.

This work makes use of global magnetohydrodynamic (MHD) simulations, which are validated by in situ Van Allen Probes (Mauk et al., 2012) observations, to investigate the large-scale interaction between Earth's magnetosphere and an MC-type structure that arrived at Earth on 27 May 2017. Specifically, we assess the impact the MC-type structure had in the equatorial IM in terms of the intensification of electromagnetic waves in the 0.5–16.6 mHz frequency range which falls within the lower spectrum of the ULF range. Additionally, the conversion among three energy forms, namely, magnetic, internal, and kinetic energies is also analyzed in the same region where the ULF waves are intensified as a result of the MC-type structure arrival. This study allows us to obtain physical information on the global distribution of the energy conversion rate and the intensification of ULF waves during different stages of the MC interaction with Earth's magnetosphere.

This paper is divided as follows: Section 2 presents the solar origins of the MC-type magnetic structure, as well as a brief discussion of the interplanetary structure as seen by the DSCOVR satellite. Section 3 discusses observations at selected intervals of the inner magnetosphere's response in terms of ULF wave generation. The methodology is presented in Section 4 as well as the definition of the configuration of the model and the technique

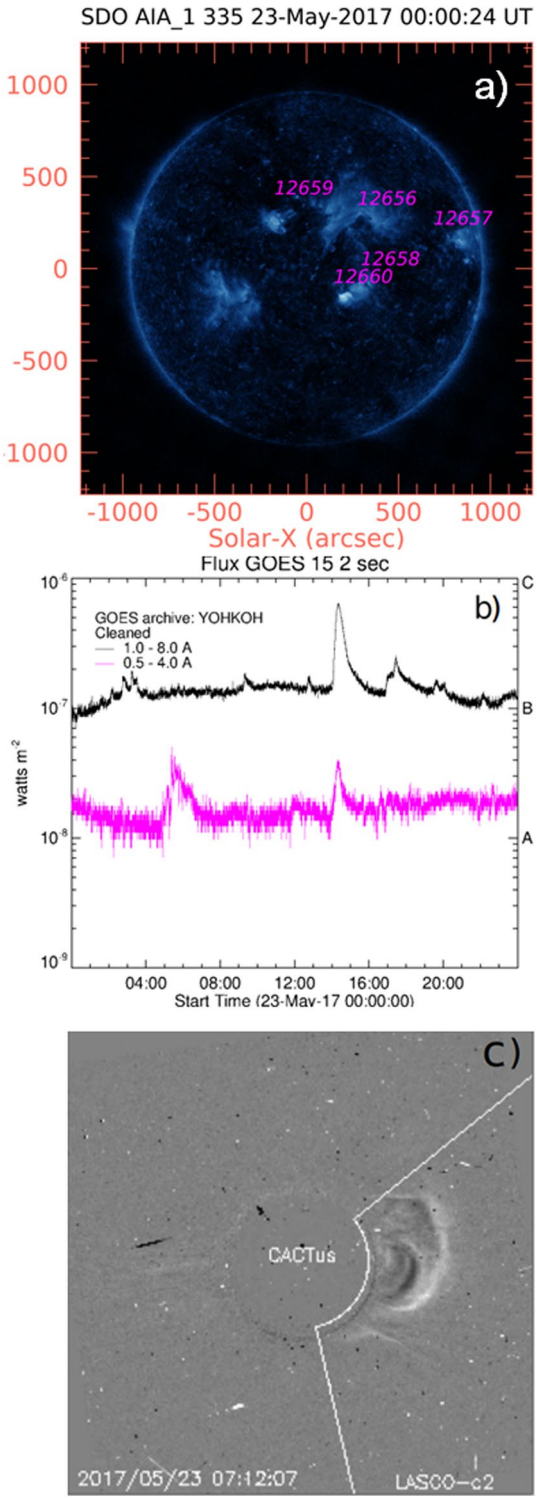

Figure 1. Disposition of active regions on the solar disk recorded on 23 May 2017 (b) Soft X-ray flux from GOES 15 satellite with a 2-s temporal resolution. (c) LASCO's coronagraph two field-of-view image of the coronal mass ejection with initial observation at 05:36 UT on 23 May 2017.

used to analyze the results. The MHD results and discussions are presented in Section 5. Finally, a summary, conclusions, and future ideas are presented in Section 6.

2. ICME Propagation and Global Magnetospheric Activity

Throughout 23 May 2017, five active regions on the solar disk were recorded. Figure 1 shows the Sun observed at 335 Å by the Atmospheric Imaging Assembly (AIA) onboard the Solar Dynamic Observatory (SDO) (Lemen et al., 2012). The channel 335 Å comes from the *Fe* XVI line 335.41 Å which highlights the active regions (O'Dwyer et al., 2010). The locations of the sources of the active regions are shown in Figure 1a. In the GOES 15 satellite records, Figure 1b, only one solar flare was detected on 23 May 2017. Event SOL2017-05-23 (B4.4) started at 14:04 UT and peaked around 14:21 UT. The event origin was from the active region 12660 NOAA (S12W21). At around 05:00 UT on 23 May 2017, a type II halo CME was detected on LASCO's C2 coronagraph, as shown in Figure 1c. Table 1 shows the parameters from the CME detected by the Computer Aided CME Tracking (CACTUS) algorithm. According to the Space Weather Database Of Notifications, Knowledge, Information (DONKI, https://kauai.ccmc.gsfc.nasa.gov/DONKI/), and the AIA instrument onboard the SDO the CME was observed at a 193 Å dimming from the active regions 12660 and 12658. Information from the CME analysis at DONKI to a distant 21.5 solar radii that occurred around 15:27 UT showed the following parameters: 12.0° longitude and—7.0° latitude in Heliocentric Earth Equatorial coordinates, and radial velocity of 375 km/s. These results were obtained using data from STEREO-A through the Space Weather Prediction Center CME Analysis Tool (SWPC CAT https://webserver1.ccmc.gsfc.nasa.gov/swpc_cat_web/). These CME parameters are the inputs of the WSA-ENLIL + Cone model. The simulation result (not shown) indicates that the flank from CME would reach the Lagrangian L1 point at about 2017-05-26T18:00Z (±7 hr). The model predicted a glancing blow with the arrival of the shock at Lagrangian L1 point on 2017-05-26T18:00Z (±7 hr). This model prediction is somewhat close to the actual time, that is, 2017-05-27T14:45Z, the interplanetary CME (ICME) shock arrived at the Lagrangian L1 point as recorded by instrumentation onboard the DSCOVR spacecraft (DSCOVR, https://www.nasa.gov/planetarymissions/discovery.html).

Figure 2 shows an overview of the solar wind parameters observed by DISCOVR spacecraft (panels a–c) of the May 27–29 MC event along with other two indicators that provide us with an idea of the impact the MC had upon the Earth's magnetosphere. The first three parameters are (panel a) the North-South (B_z, red line), and East-West (B_y, blue line) components of the IMF in the Geocentric Solar Magnetospheric (GSM) coordinate system, and its magnitude shown as a black line, (panel b) the solar wind dynamic pressure, and (panel c) the solar wind speed. The aforementioned indicators are (panel d) the magnetopause's stand-off distance in Earth radii as given by the(Shue et al., 1998) empirical model, and (panel e) the Akasofu's parameter (Akasofu, 1981; Perreault & Akasofu, 1978) which is a proxy for the energy input in the Earth's magnetosphere. We analyzed MHD results regarding energy conversion and ULF wave generation during seven 2-hr long periods delimited by the seven pairs of vertical black lines in Figure 2 and numbered from 1 to 7 on the top of Figure 2e. Each of these 2-hr long periods features different stages of the MC's interaction with Earth's magnetosphere. The first

Table 1
Parameters Observed by CACTUS (Computer Aided CME Tracking) of the Coronal Mass Ejections (CME) Took Place on 23 May 2017, at 05:36 UT

T0 (UT)	Principal angle (degree)	Angular width (degree)	Median velocity (km/s)	Lowest velocity detected within the CME	Highest velocity detected within the CME	Halo
2017/05/23 05:36	251	116	192	121	262	II

interval, which goes from 13:30 UT to 15:30 UT on May 27, presents the background solar wind conditions prior to the MC's arrival at Earth's magnetosphere. They are characterized by typical solar wind conditions at 1 AU, that is, IMF magnitude of ∼3 nT, the particle number density of about 5/cm^3 (not shown), and a somewhat slow solar wind speed reaching 304 km/s.

The average dynamic pressure of ∼1.0 nPa during the first interval is the lowest of all seven analyzed intervals. The following, that is, the second interval *I*2 has been taken inside the MC's sheath region where the IMF magnitude, alongside both IMF B_y and B_z components, have shown increased levels of fluctuations. The dynamic pressure during this interval steadily increased from ∼10 nPa to about 20 nPa thus significantly compressing the dayside magnetopause, as indicated by the Shue et al. (1998) model in Figure 2d, which showed that the magnetopause stand-off location should have moved inwards to less than 8 R_E. The third interval *I*3 in Figure 2 presents a transition region between the MC's sheath and the MC region itself, with the dynamic pressure reaching its peak value of 23 nPa, and afterward decreasing abruptly to about 7 nPa, accompanied by the IMF B_z which turned southward and remained at elevated levels of ∼−17 nT for the remainder of the interval. Intervals 4 through 7, which are taken inside the MC itself where the magnetic field in the YZ_{GSM} plane rotates smoothly, are characterized by somewhat similar driving with respect to IMF magnitude (∼13 to ∼19 nT) and solar wind

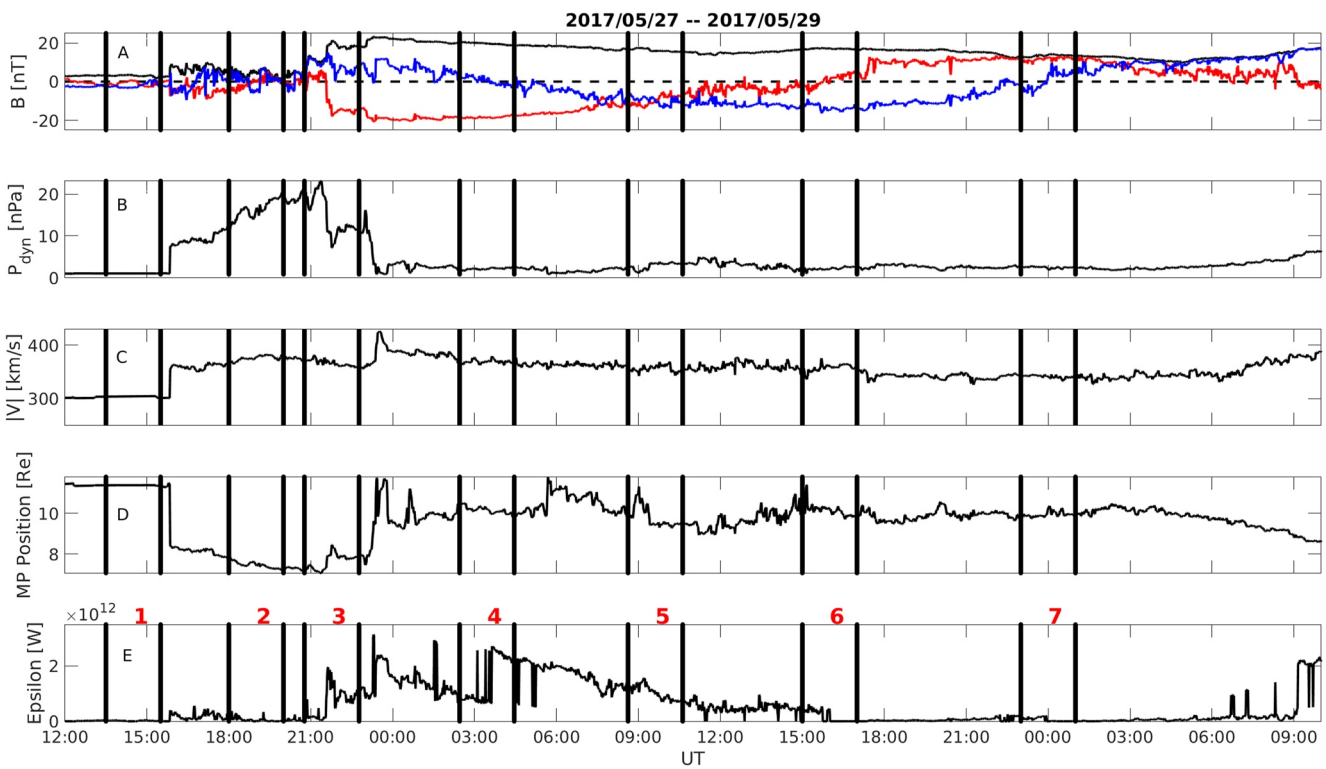

Figure 2. Solar wind parameters for event 27–29 May 2017. In the first row in black it illustrates the interplanetary magnetic field magnitude, in blue color the B_y component and in red color the B_z component. The dynamic pressure of the solar wind is illustrated in the second row. The third shows the solar wind speed. The fourth row illustrates the position of the terrestrial magnetopause as given by the Shue et al. (1998) empirical model. The last row shows Akasofu's epsilon (ϵ) parameter (Akasofu, 1981). The vertical black lines delimit the seven 2-hr long intervals where our analysis will follow. Panels (a–c) were obtained from the DSCOVR satellite. The panels (d, e) are results of analytic equations that use data from the Satellite as input parameters. https://ccmc.gsfc.nasa.gov/requests/GetInput/get_dscovr_L2.php.

dynamic pressure (∼2.4 nPa). The main difference among them is the average IMF clock angle defined by $\tan^{-1}(B_y/B_z)$. From interval 4 through 7 it goes, respectively, from ($I4$) ∼ 180°, that is, a due southward IMF with average $B_z \sim -18\ nT$, then ($I5$) to ∼225°, with average $B_z \sim B_y \sim -10\ nT$, then ($I6$) to ∼270°, an essentially purely dawnward IMF with average $B_y \sim -13$ nT, and finally ($I7$) to ∼360°(or ∼0°), a due northward IMF with average $B_z \sim 12$ nT. In what follows, we discuss Van Allen Probes electromagnetic field observations in the ULF range at selected key intervals in order to assess the IM's response in terms of ULF wave generation.

3. Inner Magnetosphere Response to the MC-Like Structure: Van Allen Probes Observations

On one hand, the role of the ULF waves in the high-energy electron flux variability within the outer radiation belt has been widely discussed in the last decades(e.g., Da Silva et al., 2019; Da Silva, Shi, Alves, Sibeck, Marchezi, et al., 2021; Da Silva, Shi, Alves, Sibeck, Souza, et al., 2021; Elkington, 2006; Friedel et al., 2002; Jaynes et al., 2015; Lejosne & Kollmann, 2020), principally due to the observations provided by several missions such as SAMPEX (Baker et al., 1993), Van Allen Probes, and Arase(Miyoshi et al., 2018). On the other hand, energy conversion between magnetic, kinetic and internal energies, and its relationship with ULF waves intensification in the outer radiation belt is not presently understood. In this work, we provide MHD results (presented in Section 5) that might aid in the likely connection between these two phenomena. Van Allen Probe's observations are used here only to validate our global MHD results. To compare them with observational data we use data from the level 2 Electric Field and Waves (EFW) instrument(Wygant et al., 2013) onboard Van Allen Probe A(Mauk et al., 2013). Figure 3 shows the ULF wave's electric field spectrograms, that is, their power spectral densities (PSDs) of the azimuthal electric field component (E_ϕ) for the analyzed period. This electric field component is chosen because it is one of the main ingredients responsible for triggering the radial diffusion mechanism (see, e.g., Ozeke et al., 2014), which is essential to causing high-energy electron flux variability within the outer radiation belt.

The azimuthal component E_ϕ is obtained from the conversion from the SM coordinates, in the Cartesian coordinate system, to polar coordinates—since the E_x component in the mGSE coordinate system is not provided in the L2 EFW data, we used the fluxgate magnetometer data from the Electric and Magnetic Field Instrument Suite and Integrated Sciences (EMFISIS) (Kletzing et al., 2013), along with the assumption that $\vec{E} \cdot \vec{B} = 0$ to compute the E_x component. Then, the signal of E_ϕ is filtered in the ULF frequency range from 1.6 to 16.6 mHz, essentially the same is used in the MHD results presented in Section 5, that is, from 0.5 to 16.6 mHz. Finally, a windowed Fourier transform is applied to the E_ϕ time series giving the PSD of the signal, presented in Figure 3 (for the whole period) and Figure 4 (for the defined 2 hr seven intervals).

The azimuthal electric field spectrogram presented in Figure 3 shows a strong power between 16:00 UT on 27 May and 15:00 UT on 28 May, which encompasses the time period of intervals 2 through 6 in Figure 2. It means that the enhancement of the ULF wave activity occurs under the influence of the MC-type solar wind structure, and it is important to compare the ULF wave observational data with the modeled data for each interval. The

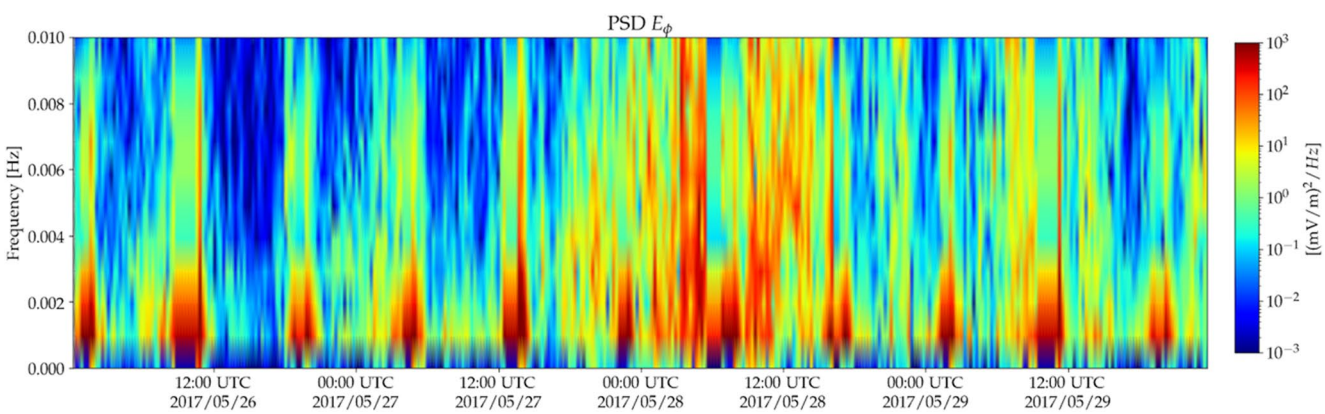

Figure 3. Van Allen Probe A ultra-low frequency power spectral density for the azimuthal (E) electric field component during the period when the Earth's magnetosphere was under the influence of the MC-type structure. Horizontal axis goes from 00:00 UT on 26 May 2017 to 00:00 UT on 30 May 2017.

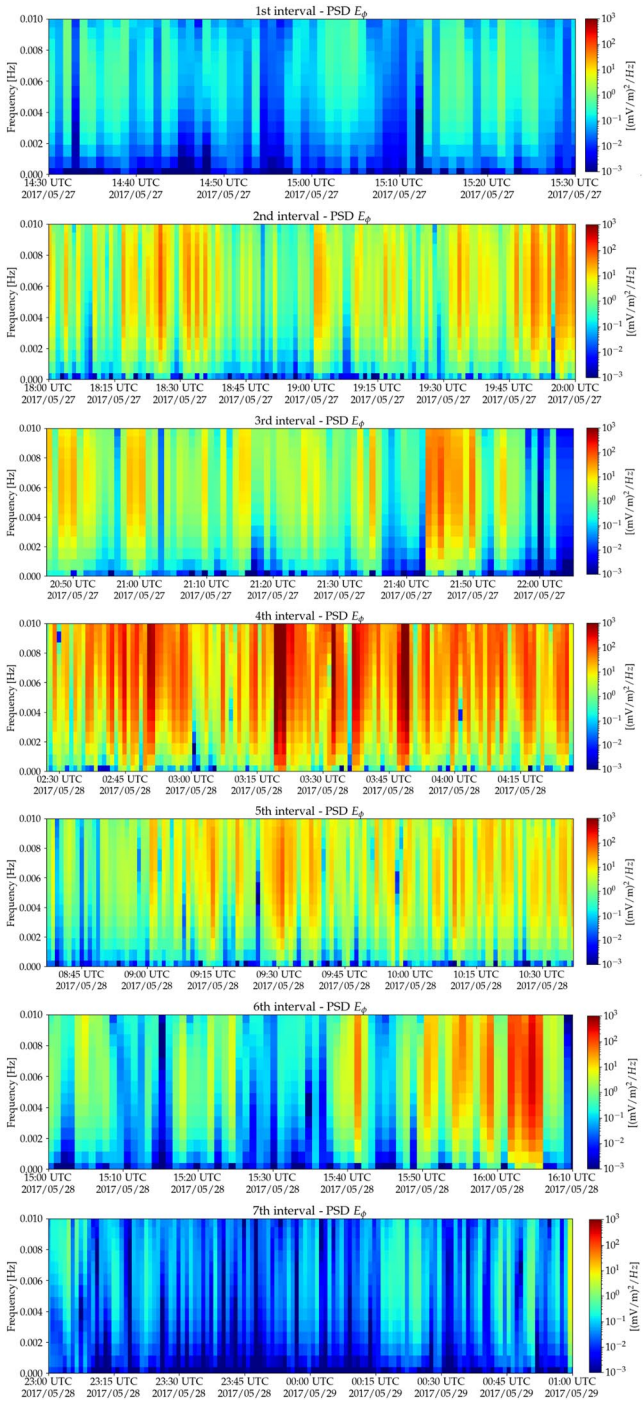

Figure 4. Van Allen Probe A ultra-low frequency power spectral density for the azimuthal (E_ϕ) electric field component for the 1st to 7th intervals depicted in Figure 2. The electric field was measured by the electric field and waves Instrument onboard the Van Allen Probes A.

10 hr-duration periodic PSD pattern that appears in Figure 3 with PSD values larger than about 10^2 (mV/m)^2/Hz and at observed frequencies in the 0 and 3 mHz range refers to the Van Allen probe A perigee, and it should be disregarded in the following analysis.

The modeling results can be considered reliable when the ULF's PSDs are similar to modeled data, considering each interval analyzed. Thereby, Figure 4 (from top to bottom) presents the ULF wave's electric field spectrograms for the 1st to 7th intervals. As expected, the first interval (first panel from top to bottom), which goes from 13:30 UT to 15:30 UT on 27 May, presents weak ULF power spectral density (PSD) in response to the background solar wind conditions prior to the MC-type structure's arrival at Earth's magnetosphere. This observational result is compatible with the MHD model, as will be shown in Section 5, where it shows essentially no intensification of the ULF power in the equatorial magnetosphere in the 3 R_E to 9 R_E radial distance range. The second interval (second panel) has been taken inside the MC's sheath region, in which the ULF PSD increases significantly coincident with the fluctuation in the IMF B_y and B_z components and the strong compression at the dayside magnetopause.

The ULF PSD within the third interval (third panel) is also strong as it has been driven by the substantial variation of the dynamic pressure within a transition region between the MC's sheath and the MC region itself (see more details of the mean values of plasma parameters in the Appendix A). The MHD model results also show an increase for both 2nd and 3rd intervals. The ULF PSD measured from the EFW instrument within the fourth interval (fourth panel) is considered very strong compared with other intervals and occurs inside the MC itself. Although intervals 4 through 7 are taken inside the MC itself, the ULF PSD both measured and modeled in these intervals decreases significantly compared to the measured ULF PSD on the 4th interval, principally in the 7th interval, which is similar to the 1st interval. It means that during the 7th interval, the MC-type structure effects in the IM have already decreased considerably. Before presenting the MHD results in Section 5, the following section describes the methodology used for acquiring the modeling results.

4. Methodology

In Section 4.1 a brief introduction to the subject related to numerical simulation is made and the global MHD model used is presented, as well as the particular configuration used in this paper. In Section 4.2 we will present in more detail the methodology used to analyze the modeled data regarding ULF waves and energy conversion.

4.1. Global MHD Simulation

In plasma physics, the vast majority of systems of equations cannot be solved by conventional techniques. They do not have an analytical solution, and only under certain arguments, simplification, and considerations can we arrive at a sketch of the behavior of such systems of equations. The ideal MHD equations, which incorporate the conservation laws and Maxwell's equations and that consider the plasma as a conducting fluid, are from the class of nonlinear systems of equations without an analytical solution; we can only obtain approximated solutions through numerical techniques. In view of the complexity of understanding the physical processes occurring in the

magnetosphere, ionosphere, and upper atmosphere only by means of observational data, space scientists have made efforts to develop global MHD models of the interaction of the solar wind with the Earth's magnetosphere. These models are self-consistent and can provide information on global physical processes in different spatial regions and time intervals and, at the same time, simulate scenarios with numerical experiments that either use as input parameters synthetic solar wind data or actual solar wind data provided by satellites orbiting the Lagrangean L1 point at approximately 1.5 million km away from Earth (Janhunen et al., 2012; Lyon et al., 2004; Ogino et al., 1994; Raeder et al., 2008; Tanaka, 1995; Tóth et al., 2012; Wang et al., 2013; Zhang et al., 2019). The vast majority of these global MHD models used by the scientific community are coupled to another magnetosphere, ionosphere, and upper atmosphere models in order to better represent the physical processes in each region since ideal MHD does not take into account the kinetic physical processes of wave-particle interaction and the movement of particles in complex field configurations, essential for understanding RC and radiation belt dynamics (Fok et al., 2014). In this work, we use the ideal version of the model SWMF/BATS-R-US (De Zeeuw et al., 2004; Gombosi et al., 2001, 2003, 2021; Tóth et al., 2005; Tóth et al., 2012, and references therein) global MHD code, developed at the University of Michigan in the Center for Space Environment Modeling (CSEM) and available at the Community Coordinated Modeling Center (CCMC/NASA). In order to have a better representation of the physical coupling processes of the MC-type structure, we chose to use three components of the SWMF/BATS-R-US, namely, GM (Powell et al., 1999), IM (specifically the Rice Convection Model—RCM (Toffoletto et al., 2003)), and the ionosphere electrodynamics (IE) modules (Ridley et al., 2006).

Due to its versatility, the SWMF/BATSRUS model allows the user to dynamically focus the grid resolution following physical parameters such as gradients, or maintain the arrangement of blocks with fixed resolution levels in a given region. For this research, we used the Geocentric Solar Magnetosphere (GSM) coordinate system and the choice of adaptive blocks arrangement was fixed, where we concentrated the $\frac{1}{4}$ R_E resolution in a region with dimensions of $-32 < x < 12$, $-12 < y < 12$, and $-7 < z < 7$. With this configuration, the domain includes all of the equatorial nightside and dayside regions where we will carry out the study of energy conversion together with the dynamics of ULF waves. The other configured parameters such as the Pedersen conductivity, simulation domain, temperature, and density at the inner boundary of the model follow the same settings as in Jauer et al. (2019).

4.2. Integrated Power Spectral Density and Energy Conversion

In order to carry out the analysis and obtain a better understanding of the effects of the 46-hr long interaction of the MC-type structure with the GM, more specifically at the equatorial region $z = 0$, the following steps have been performed: as mentioned in Section 2, seven 2-hr long intervals, namely, $I1$ to $I7$ (see Figure 2-e), have been selected, and they feature different stages of the MC-type structure's interaction with Earth's magnetosphere. For each of these intervals, a spatial domain in the equatorial plane has been defined in polar coordinates (R, ϕ) with $3 \leq R \leq 9\ R_E$ and $0 \leq \phi < 360$. This region has been discretized with equally spaced steps of $dR = 0.06\ R_E$ and $d\phi = 3.6°$, covering 24 hr in Local Time (LT). ULF wave intensification and energy conversion(transfer) are both analyzed in this equatorial region. The set of equations that describe the energy balance between the magnetic, kinetic, and thermal energy and the energy conversion terms are presented below (Birn & Hesse, 2005):

$$\frac{\partial}{\partial t}\frac{B^2}{2\mu_0} = -\nabla \cdot \left(\frac{\vec{E} \times \vec{B}}{\mu_0}\right) - \vec{V} \cdot \left(\vec{J} \times \vec{B}\right) - \vec{J} \cdot \vec{E}' \tag{1}$$

$$\frac{\partial}{\partial t}\frac{\rho V^2}{2} = -\nabla \cdot \left(\frac{\rho}{2} V^2 \vec{V}\right) + \vec{V} \cdot \left(\vec{J} \times \vec{B} - \nabla P\right) \tag{2}$$

$$\frac{\partial u}{\partial t} = -\nabla \cdot \left[(u + P)\vec{V}\right] + \vec{V} \cdot \nabla P + \vec{J} \cdot \vec{E}' \tag{3}$$

Equation 1 describes the transport of magnetic energy and is derived through Faraday's law together with Ampère's law following some mathematical manipulations and assuming that the electric field in the plasma rest frame $\vec{E}'$ is given by: $\vec{E}' = \vec{E} + \vec{V} \times \vec{B}$. The two terms to the right of Equation 1 were derived by replacing the electric field $\vec{E}$ with $\vec{E}'$ in $\vec{E} \cdot \vec{J}$ in the original equation presented by Birn and Hesse (2005). The physical implications of writing the electric field in this reference frame are related to the possibility of the emergence of

an electric field beyond the ideal regime. These implications occur not only due to the convection of plasma but also due to the other effects that follow the generalized Ohm's law (Vasyliunas, 1975), in which this electric field is correlated with non-ideal effects and the physical process of magnetic reconnection. In this work, we use an ideal version of the SWMF/BATSRUS model, that is, the electric field in the plasma rest frame is assumed to be zero, which implies that resistivity effects are not considered, and the term $\vec{E}' \cdot \vec{J}$ representing ohmic dissipation is considered zero in Equations 1 and 3. However, the MHD models may generally present some non-ideal effects that mimic physical resistivity, which is purely numerical in nature. Global MHD models in general are designed to minimize these effects, and there is no clear and precise way to measure such effects due to their complexity. In general, the physical effects are more relevant than the numerical ones. The discussion about these effects is outside the scope of this work. The Equation 2, which represents the kinetic energy flux transport through the divergence and its conversion, can be derived with the help of the momentum equation and mass conservation equation following some mathematical steps (Birn & Hesse, 2005). Usually, the kinetic energy equation tells us that the temporal variation is associated with its transport through the flux term, the first term on the right, and the conversion term that is associated with the magnetic force and pressure gradient. Equation 3 represents thermal energy transport. It is obtained by subtracting the equation representing the conservation law of total energy from Birn and Hesse (2005) with Equation 2. In this way, the temporal variation of the thermal energy term on the left side of the equation is associated with the divergence of the enthalpy flux $\left((u+P)\vec{V}\right)$, and the $\vec{V} \cdot \nabla P$ term. The term that represents the ohmic dissipation effect, as explained above, is considered zero, that is, in an ideal MHD regime the only way to increase or decrease the internal energy is through the compression of the plasma (Keesee et al., 2021; Schindler, 2006).

Three types of energy densities which correspond to the terms to the right-hand side of Equations 1–3 in the MHD approximation are analyzed here, namely, magnetic (E_m), internal (E_i) and kinetic (E_k) energies (Birn & Hesse, 2005; Ebihara & Tanaka, 2017, 2020), and their equations are defined in units of (nW/m^3) as follows:

$$E_m = -\vec{V} \cdot \left(\vec{J} \times \vec{B}\right), \tag{4}$$

$$E_i = \vec{V} \cdot \nabla P, \tag{5}$$

$$E_k = \vec{V} \cdot \left(\vec{J} \times \vec{B} - \nabla P\right), \tag{6}$$

where $\vec{V}$ is the plasma bulk velocity, $\vec{B}$ is the magnetic field vector, $\vec{J}$ is the plasma current density as derived from Ampère's law, and P is the plasma pressure. Notice that Equations 4–6 has dimensions of energy density flux, that is, Watt/m^3, but hereafter we will refer to them only as either of the three energy forms mentioned above, that is, magnetic energy, kinetic energy, and internal energy. The physical quantities E_m, E_i, and E_k can assume both positive and negative values. Positive values mean that the physical quantity is increasing its energy at the expense of decreasing the others or the combination of the others. We'll show it in more detail in the color map and temporal profiles in the Section 5.

To obtain the poloidal (E_ϕ) and toroidal (E_r) components of the electric field, as well as the energy conversion terms expressed in Equations 4–6, we sampled the MHD model output variables, that is, $\vec{V}$, $\vec{B}$, $\vec{J}$ and P, at a time cadence of 30s, thus for each point of the discretized equatorial domain a 2-hr long time series of each of the MHD model output variables has been obtained with each time series having 240 elements. Then, the electric field was calculated as the vector product of the velocity and the magnetic field and rotated to an appropriate mean field-aligned coordinate system, as done by Jauer et al. (2019), that gives rise to the already mentioned poloidal and toroidal components of the electric field. Since the sampling frequency f_s of all the time series is $f_s = 1/30s = 33.3$ mHz, the highest resolvable frequency in our MHD analysis is $f_s/2 = 16.6$ mHz. The MHD model electric field fluctuations are evaluated in the 0.5–16.6 mHz range by applying a Fast Fourier Transform (FFT), as done by Claudepierre et al. (2008), in each electric field component time series. As a result, a PSD in units of (mV/m)^2/Hz is obtained for each component, that is, PSD_{E_ϕ} and PSD_{E_r}, at each point of the discretized equatorial domain. The PSD_s are then integrated in the (0.5, 16.6) mHz range at each point of the domain generating the integrated PSD, or integrated power spectral density ($IPSD$), as follows:

$$IPSD_{\phi,r} = \int_{0.5}^{16.6\ mHz} PSD_{E_\phi,E_r}\, df, \qquad \text{units of (mV/m)}^2. \tag{7}$$

In this way, we obtained for each of the seven 2-hr long intervals defined in Figure 2e a map of the spatial distribution of the electric field wave power integrated in the lower frequency spectrum of the ULF wave range. The energy conversion/transfer terms are calculated as the composition of the MHD output variables mentioned above at each point of the discretized domain. It should be noted that our analysis is restricted exclusively to variations over the equatorial $z = 0$ plane, that is, only the x and y components of the vectorial terms in Equations 4–6 are actually used, and also only the x and y components of the $\vec{J} \times \vec{B}$ term:$\left(\vec{J} \times \vec{B}\right)_x = J_y B_z - J_z B_y$, $\left(\vec{J} \times \vec{B}\right)_y = J_z B_x - J_x B_z$. Regarding the spatial and temporal distribution of the energy conversion terms, we have a spatial slice (for each energy term) at each time interval of 30s, which means 240 slices per energy term for each of the seven 2-hr long intervals. In order to obtain a spatial slice, for a given energy term, that could be representative of the 2-hr long interval, we calculated the median value of the given energy term at each point of the discretized domain, thus resulting in a single slice per interval for that energy term. We can then visually compare such a slice with the IPSD maps of E_ϕ and E_r. We show in the next section that the median approximates reasonably well the temporal distribution of energy conversion along the equatorial plane of the modeled IM.

5. Results and Discussions

5.1. MHD and Van Allen Probes Data Comparison

This section aims to show the comparison made between the poloidal component E_ϕ of the electric field obtained by both the spacecraft A of the Van Allen Probes (RBSPA) and the one modeled by the SWMF/BATSRUS. Their time series are shown in Figures 5 and 6. The E_ϕ time series for the MHD model has been acquired along the orbit path of RBSPA for the several intervals analyzed in this study (see Figure 6c for orbit details).

Figure 5a depicts the comparison for the interval $I1$, which goes from 14:30 UT to 15:30 UT, and it is related to the quiet solar wind conditions. The red curve is for the MHD model whereas the black one is for RBSPA. As expected, the level of fluctuation in the IM is quite low for both model and observed cases, and more importantly the MHD model and RBSPA observations agree quite well in order of magnitude. This feature is actually present for all the intervals shown in Figures 5 and 6.

Figure 5b shows the comparison for interval $I2$, which represents the region of the magnetic sheath during the compression of the magnetosphere. Although the RBSPA interval in Figure 4b goes from 18:00 UT to 20:00 UT, the comparison was performed only for the last hour of the interval because before ∼19:00 UT the spacecraft radial distance was below 3 R_E (see Figure 6-c) which lies outside of the spatial domain adopted for analyzing the MHD data, which is $3 \leq R \leq 9\ R_E$. Even so, both modeled and observed data are quite consistent with one another.

The interval $I3$ that is shown in Figure 5-c represents the already disturbed conditions where the global and IM is still under the effect of an intense dynamic pressure of the solar wind and the IMF component changes its direction to southward B_z. We can verify again that both profiles are oscillating practically on top of each other with a small difference in amplitude.

The $I4$ interval as seen in Figure 6c is completely below $R < 3$ thus, as well as part of the $I2$ interval we did not perform the comparison for the reasons already explained above. The interval $I5$ that represents the time interval where the components B_y and B_z are oscillating with average values close and also starts the storm recovery phase. In this interval, as in the others, we can again see that both profiles are oscillating close with a slight perturbation in the initial part of the interval in the data of the MHD model.

The last interval to be analyzed is the $I6$ where the predominant component of the IMF is B_y and it is fully in the storm recovery phase. We can see that both the modeled profiles compared point to point and those from the RBSPA are in general agreement and oscillate with close values. Regarding the $I7$ interval below, we will show the reasons for not analyzing this interval in particular. In our analysis regarding the point-to-point comparison between the real data from the RBSPA and the modeled data provided by the MHD model, they are shown to be in agreement and consistent.

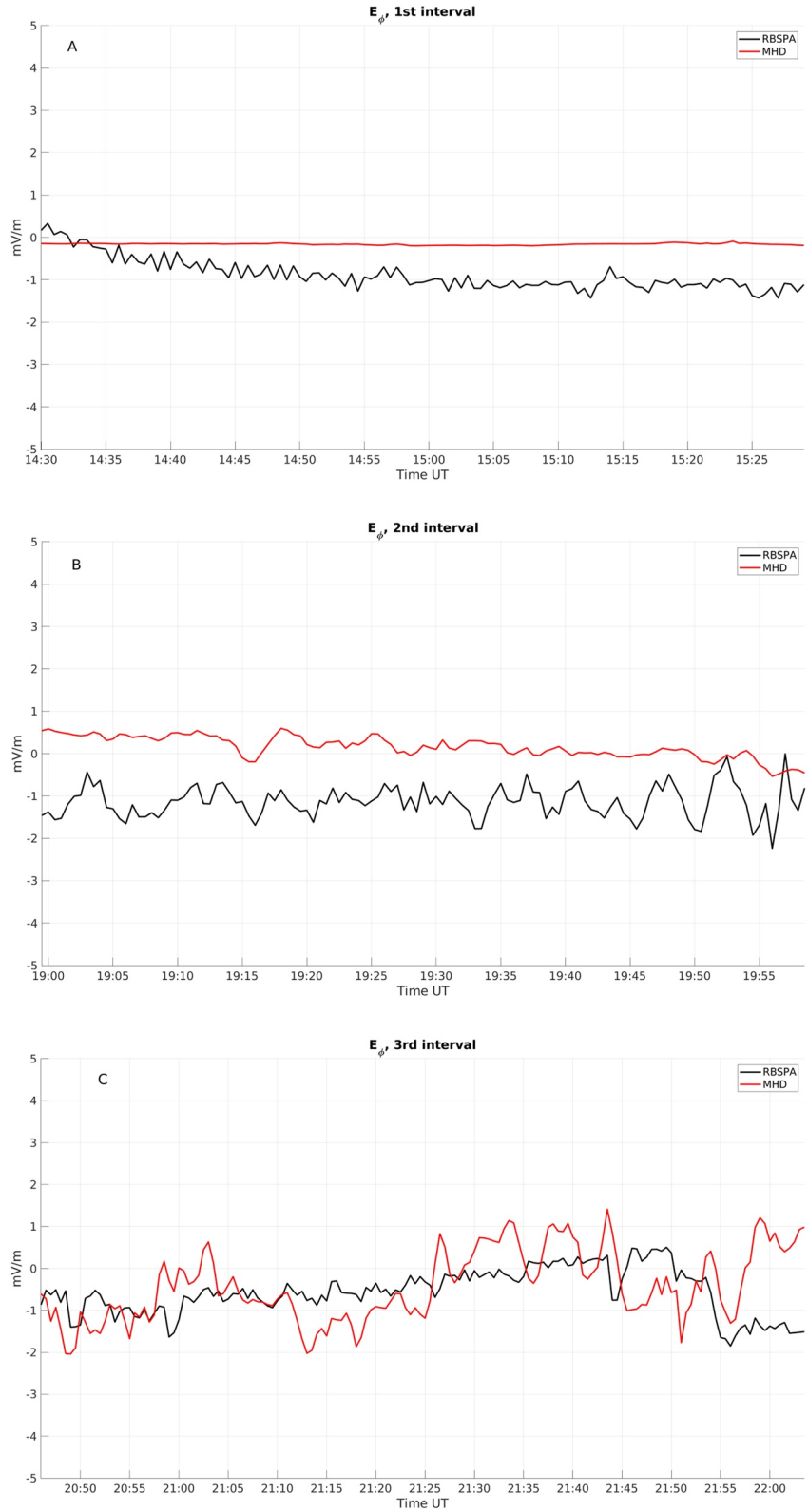

Figure 5. Comparison between Van Allen Probes (RBSPA, black) and global magnetohydrodynamic (MHD) model results (MHD, red) for intervals *I*1 through *I*3. Observational results are plotted only when the spacecraft is above a radial distance of 3 R_E. Refer to Figure 6c for details of Van Allen Probes' orbit path.

Figure 6. Same as Figure 5 but for intervals *I*5 (panel a) and *I*6 (panel b). Panel (c) shows Van Allen Probes' orbit paths during intervals *I*1, *I*2, *I*3, *I*5, and *I*6, along with the inner boundary (black circle) of the magnetohydrodynamic model.

5.2. MHD Model Results

Before starting the discussions of the results we will make a brief comment regarding the interval *I*7. This interval represents the interaction of the interplanetary structure whose IMF configuration B_z is mostly northward. We found that with the choice of the limits of the color bar and also of the limits of the components E_ϕ and E_r of the IPSD, both the intervals *I*1 and *I*7 present qualitatively the same results, in this way, we will only analyze and present the interval *I*1.

The MC-type structure event analyzed here promoted the emergence of intense magnetic storms with SYM-H index less than −100 nT and enhanced substorm activity as probed by the auroral electrojet AE index levels, which peaked at almost 2000 nT, as seen in the bottom-most panels in Figure A1. We show in this section that the IM was energized, and the energy conversion was at a high level of activity.

Figure 7 presents the MHD results for the interval *I*1, which features the background solar wind conditions prior to the MC-type structure's arrival at the DSCOVR satellite location. The top row of Figure 7 shows the equatorial ($Z_{GSM} = 0$) maps of the magnetic E_m, internal E_i, and kinetic E_k energies on the left, middle and right panels, respectively. The energy terms are presented with the same color bar range, that is, from −0.03 to 0.03 nW/m^3. For ease of comparison among the different stages of the MC interaction with the Earth's magnetosphere, such a color bar range has been fixed for all seven analyzed intervals. This color bar range has been optimized to avoid a high saturation level of the quantities plotted in some intervals. The bottom row of Figure 7 shows the IPSD values for the poloidal (E_ϕ, left) and radial (E_r, right) MHD electric field components with a common color bar range, that is, from 0 to 9 (mV/m)^2. As with the color bars for the energy terms, the ones for the electric field components have also been kept fixed for all of the seven analyzed intervals.

Note that the median values of the energy conversion terms throughout the equatorial region are near zero in Figure 7, which is consistent with the lowest of the average values of the solar wind input power as calculated by the Akasofu's $\epsilon = 1.98 \times 10^{10}$ W (see., Table A1). Likewise, almost no ULF wave activity is detected in the first interval as far as the IPSD values of the two electric field components are concerned. Compared to the following intervals presented below, this behavior was already expected since the IMF during this period was relatively steady with no noticeable fluctuations, and both solar wind speed and density were fairly typical.

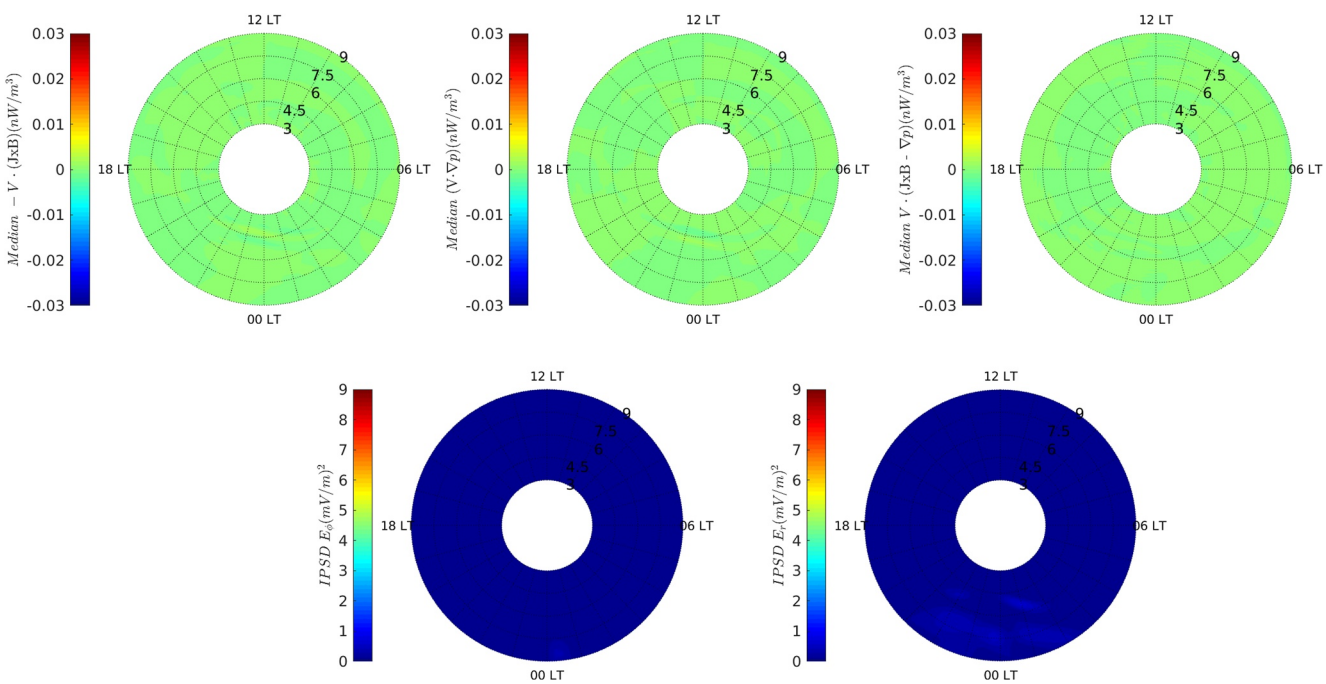

Figure 7. Represents the *I*1 interval. The first row above left to right represents the median of the magnetic energy conversion term, the second represents the internal energy conversion term, and the last term represents the kinetic energy conversion. The second row represents the integrated power spectral density of the azimuthal and radial electric field component in the equatorial plane at $z = 0$. Both the median and the integrated values were taken within 2 hr long.

As we move to the second interval *I*2, however, a drastic change is seen in all panels of Figure 8 as the magnetosphere is under a higher level of driving. The magnetosphere is greatly compressed during this interval, with the magnetopause stand-off position reaching values as low as 7.5 R_E according to Shue's model, Figure 2d. Figure 9a shows a radial profile, from 3 R_E to 9 R_E, of the above-mentioned energy forms along 15 LT for the second analyzed interval. The dayside magnetopause location can be readily distinguished in Figure 9a as both internal (E_i, red line) and kinetic (E_k, cyan line) energies reach a positive and a negative peak value, respectively, at a radial distance of ~7.8 R_E. The average IMF components B_z and B_y are oscillating with an average value of −0.5 and 0.9 nT, respectively, that is, close to zero as seen in Appendix A (Table A1).

In Figure 8, note that the internal energy mostly balances the kinetic energy with a smaller contribution of the magnetic energy in the dayside region. Thus not only at 15 LT, but in a large portion of the equatorial dayside magnetopause, specifically in the 13:30–17:00 LT and 07:00–10:30 LT ranges, the kinetic energy density from the magnetosheath flow is being converted into mostly internal energy, and to a smaller degree to magnetic energy as well. When comparing the level of electric field fluctuations at 15 LT, as probed by the IPSD, we can see in Figure 9-b that the radial (E_r) component is the one contributing the most to the IPSD of the electric field vector, particularly at the magnetopause (see, e.g., Jauer et al., 2019). We can also clearly see that the energy conversion region is close to or overlapping with the IPSD intensification regions, most evident in the toroidal (or radial) component as we can see in Figures 9a and 9b.

The energy conversion in the nightside region for 21:00 ≤ LT ≤ 03:00 and for radial distance 4.5 ≤ R_E ≤ 9.0 there is a predominance in the conversion between the internal energy and magnetic with a small contribution of kinetic energy. On the other hand, the kinetic energy conversion is mostly positive in the nightside region and its values increase moving away from the midnight meridian, tending toward the flank regions. The shape of the IPSD spatial distribution of the toroidal component on the nightside region surrounds the shape of the distribution of the medians of the energy conversion, especially the kinetic component. On the other hand, we observe that the IPSD of the poloidal component has a distributed behavior in the LT's and R's mentioned above.

The MC-magnetosphere interaction evolves through *I*2 and intensifies the energy conversion rate (due to compression of the magnetosphere), observed in the dayside and nightside regions. Additionally, it increases the IPSD. We must always keep in mind that energy transfer, MHD and electromagnetic through the Poynting vector

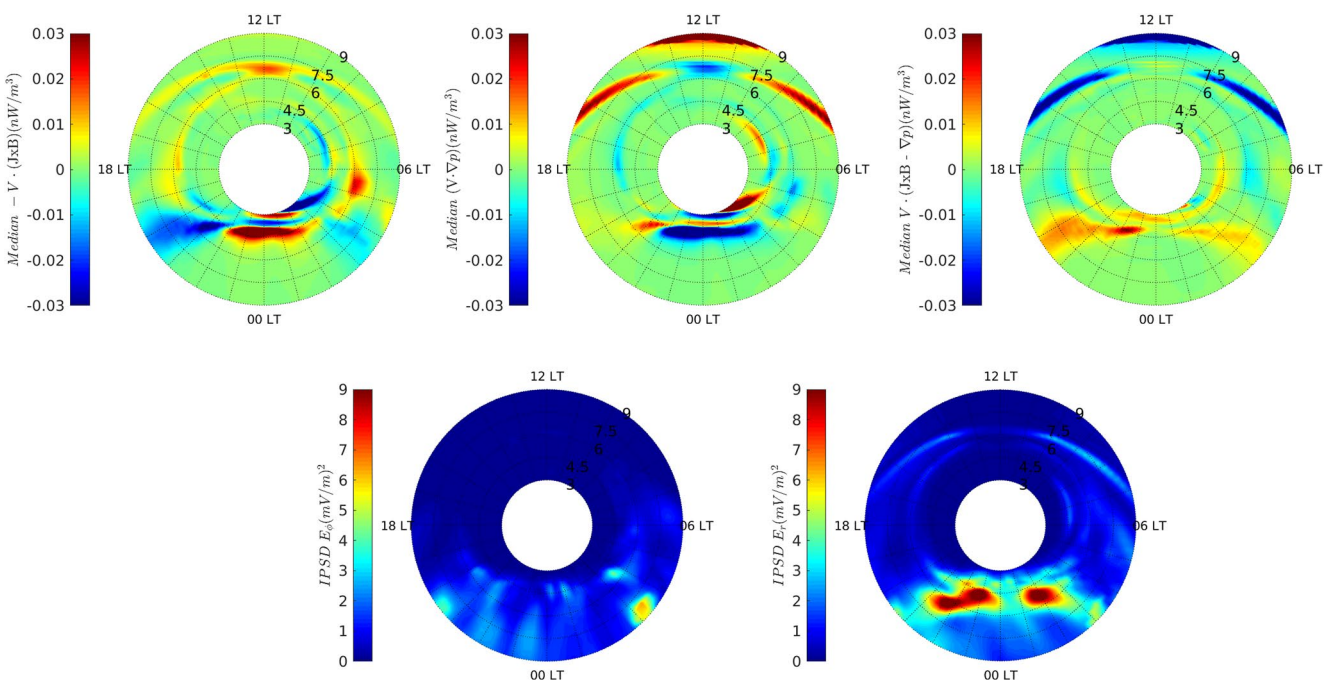

Figure 8. Represents the *I*2 interval. The first row above left to right represents the median of the magnetic energy conversion term, the second represents the internal energy conversion term and the last term represents the kinetic energy conversion. The second row represents the integrated power spectral density of the azimuthal and radial electric field component in the equatorial plane at $z = 0$. Both the median and the integrated values were taken within 2 hr long.

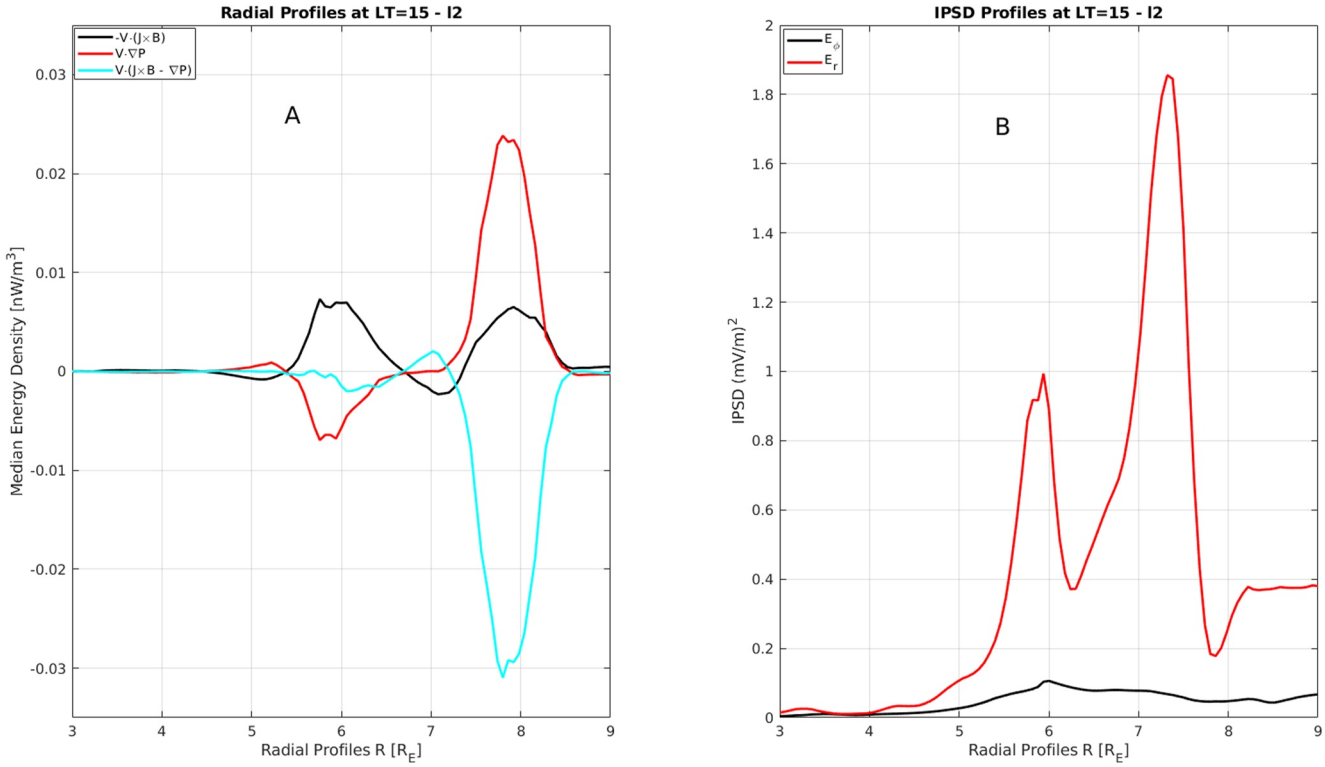

Figure 9. The first panel (a) on the left illustrates a radial profile in the interval (3 R_E, 9 R_E) of the three components of the median in Local Time (LT) 15. The second panel (b) in the right represents a radial profile, in the same LT and at the same radial distance of the integrated power spectral density for the radial and azimuthal component of the electric field.

flux, requires the specification of a contour/area orientation (see, e.g., Palmroth et al., 2003; Wang et al., 2014; Brenner et al., 2021). In this article, the analyzed terms are scalar. Therefore, they are invariant, and it does not need to specify an oriented surface or region through which the energy is converted.

In fact, during intervals *I*2 and *I*3, the magnetosphere is under the action of a high value of dynamic pressure ∼(16–14) nPa respectively (see., Table A1). The magnetosphere decreases its cross-section, as can be seen in Figure 2-d by the Shue et al. (1998) empirical model of the magnetopause stand-off distance. This abrupt compression causes an intensification in the current system that couples the outer magnetosphere with the inner one and the ionosphere. The two important current systems in the magnetosphere are the region 1 (R1) and region 2 (R2) field-aligned current systems. The R1 current system couples the magnetopause currents to the high-latitude ionosphere, where this circuit is closed by Pedersen currents.

On the other hand, the R2 current system flows along closed magnetic field lines and couples in the lower latitude ionosphere. The R2 current system is generated in the inner part of the current sheet, and the RC region (Gombosi et al., 2003). Thus, as mentioned above in Section 4, the coupling of the RCM model allows better reproduction of these inner current systems, which play a fundamental role in the transport of momentum and energy flow. It is beyond the scope of this paper to an in-depth discussion of the coupling of current systems R1 and R2, but we are aware of their importance in energy conversion and power enhancement in the ULF range as they are associated with forces exerted on the plasma. Further details on the coupling of current systems in the global and IM and the emergence of dynamo regions can be found in Tanaka (1995). Future work will be carried out to detail the relationship of this coupling.

The next interval, *I*3, is delimited by two vertical black lines in Figure 2 and indicated in panel e. This interval presents a sharp transition in the observed plasma parameters; the IMF B_z component during approximately half of the interval oscillated around some positive value, then turned southward with a maximum peak of ∼−17 nT at 21:47 UT. The dynamic pressure peaked at 23 nPa at 21:22 UT and reaches a minimum value of ∼7 nPa at

21:47 UT. The subsolar magnetopause has shifted to ~7 R_E position at 21:22 UT. The solar wind speed mainly remained constant, around 360 km/s.

Figure 10 in the first row illustrates the median of the energy terms. We can see in the color map that both on the dayside and nightside regions, but more visibly pronounced in the nightside region, there is a high level of energy conversion close to these regions with an intensification of the level of fluctuations in the frequency range of the ULF waves as represented by the IPSD. An interesting feature was found in the color map of the medians of energy conversion terms, and this pattern was more evident in the intervals *I*2 and *I*3 in the nightside region during high dynamic pressure. Note that the development of the storm (main phase) and substorm have not yet started, as can be seen in Figures A1e–A1f. The conversion rate between E_m, E_i, and E_k forms a spatial pattern starting around 19:00 LT and extending to 05:00 LT. The median shows that for radial distances (3 R_E − 6 R_E), there is an exchange of sign between the terms E_m and E_i. However, the kinetic energy remains positive, with an intensity close to zero for the 22:00 to 02:00 LT and radial distance (4.5 R_E − 9 R_E). This exchange pattern occurs mostly between the E_m and E_i components, the E_k has little contribution to the conversion in this region.

One way to check if our entire methodology is consistent is to try to find theoretical physical evidence in the results of Figure 10. To be more specific, during interval *I*3, we have an opportunity to verify this, as the Earth's dayside magnetopause region is under the influence of an intense IMF B_z due south and is still under the action of the high dynamic pressure of the ~14.6 nPa (see, Table A1) and oscillating in the vicinity between 7 R_E and 8 R_E, that is, within our domain of study.

The energy predominantly contained in the solar wind in the form of kinetic energy is first converted in the bow shock where $E_k < 0$ into magnetic energy $E_m > 0$ and the internal energy of plasma, that is, ($E_i > 0$), as a dynamo process (MHD generator) (Siebert & Siscoe, 2002). This energy, stored in the magnetic field and plasma will again be reconverted in the region of the dayside of the magnetosphere, in the magnetopause load process through the physical process of magnetic reconnection. This conversion of the energy contained in the field will accelerate the plasma and increase the internal energy, with a decrease in magnetic energy. We will look at evidence of this physical process at the medians of energy conversion and also near the approximate position of the Earth's magnetopause through a time history of the components of energy conversion over the 2-hr interval.

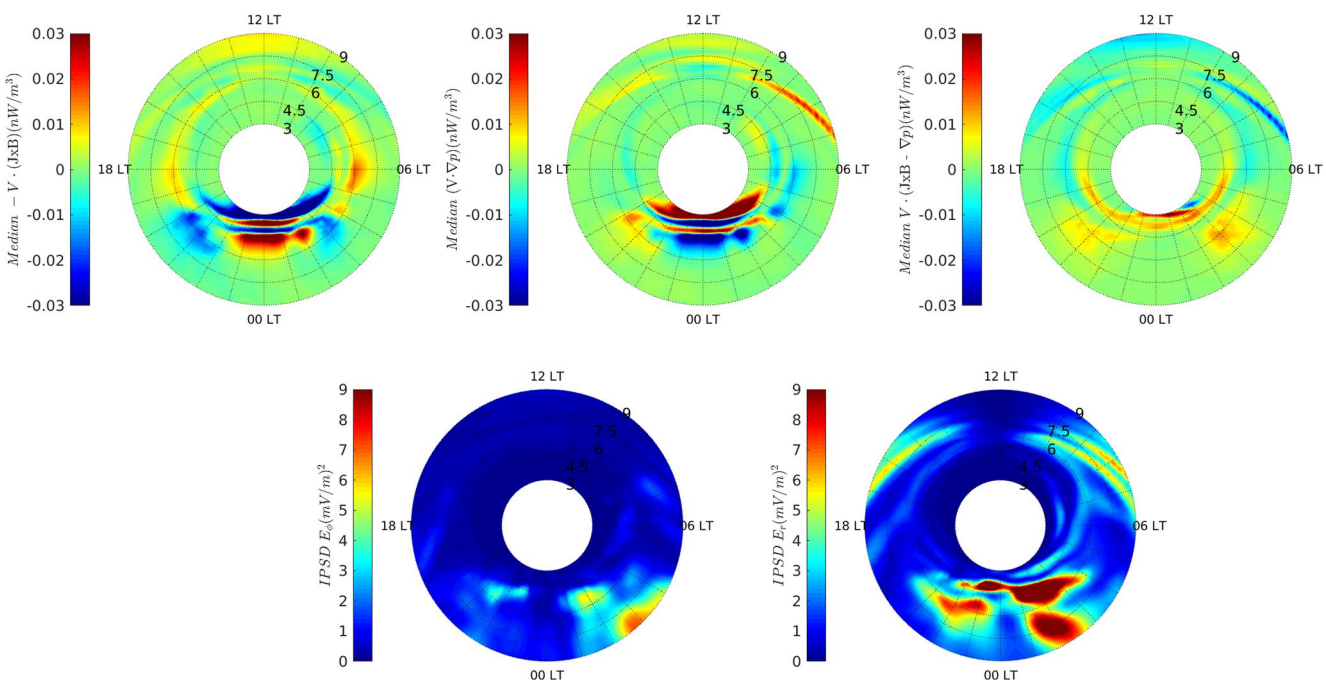

Figure 10. Represents the *I*3 interval. The first row left to right represents the median of the magnetic energy conversion term, the second represents the internal energy conversion term and the last term represents the kinetic energy conversion. The second row represents the integrated power spectral density of the azimuthal and radial electric field component in the equatorial plane at $z = 0$. Both the median and the integrated values were taken within 2 hours long.

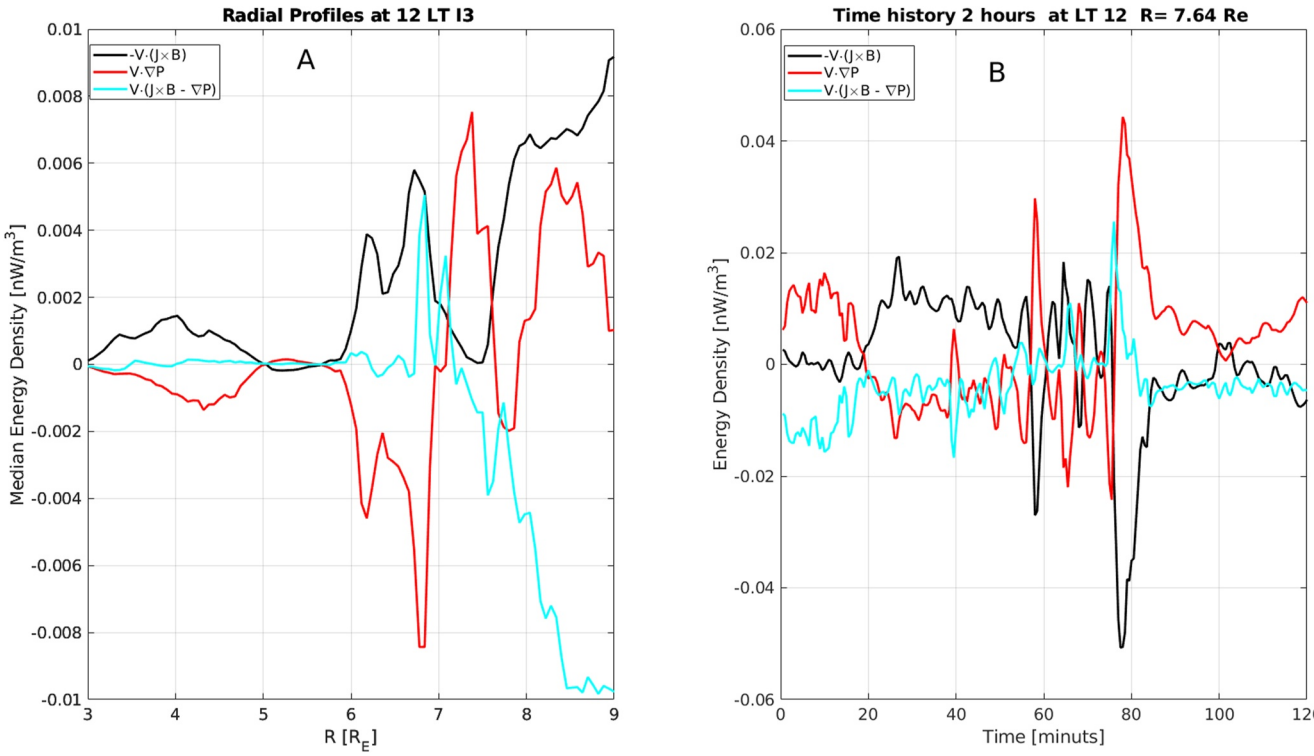

Figure 11. Panel (a) represents the radial profile ($3R_E$ to $9R_E$) in the Local Time (LT) 12 in the Sun-Earth line from the median of Kinetic, Magnetic and Thermal energy conversion. Panel (b), on the right side, represents the temporal history of three components of energy conversion extracted in the LT 12 and radial distance 7.64 R_E.

In Figure 11, which represents the response of the IM in terms of energy conversion during an interval with B_z southward, the energy contained in the magnetic field is converted into acceleration and the internal energy of the plasma around the magnetopause position. The first row left panel A represents the median of the energy conversion components extracted from (3 R_E to 9 R_E) in LT 12. The median helps us get an idea of the spatial distribution and pattern of energy conversion during each of the I's 2-hr intervals. An approximate way to check during the *I*3 interval if the energy conversion is taking place in the vicinity of the magnetopause under the influence of the southward IMF B_z configuration is to extract a temporal profile at LT 12 around the mean position 7.64 Re into *I*3. As discussed earlier, the IMF B_z component becomes predominantly south after 21:47 UT, while the magnetopause due to dynamic pressure variation does not remain in the same position. However, if we extract a time series, in the LT and *R* mentioned above we should get, after IMF orientation change, spikes in energy conversion when this setting is oscillating around position 7.64. In Figure 11b, after ∼77 min we observe a peak in the rate of conversion of magnetic energy into kinetic and internal energy, characteristic and also consistent with Load (Birn & Hesse, 2005; Ebihara & Tanaka, 2020). In this way, we find that the median of the energy conversion components, Figure 11a around the position $R = 7.64\ R_E$, is a representative amount of the energy conversion during the phase in which B_z changes orientation. An interesting feature can also be observed in Figure 11b that represents the time evolution of energy transfer between E_m, E_i, and E_k. Even limiting ourselves to a specific LT and a fixed *R*, we can notice that in the interval of ∼(0–20) minutes the energy conversion takes place between the internal and kinetic energy terms with a small contribution from the magnetic energy. Right after ∼(20–60) minutes, this setting changes and the conversion becomes mostly magnetic, the positive value means by the definition Section 4 that the field is increasing its energy at the expense of the work done by the pressure gradient and by the motion of the plasma, that is, in this region or nearby a dynamo region is emerging. In the range of ∼(60–120) minutes, due to the configuration of B_z southward this region is dissipating converting the energy stored in the magnetic field into internal and kinetic energy. What we can see is that in the same spatial region, not necessarily, a dynamo region can operate continuously, but at all times there is an exchange between load and dynamo. A physical consequence in terms of the dynamics of particles that perform movements and cross these energy conversion regions can abruptly affect the energy content of different particles that observe these regions

differently temporally. In Figure 9 panels a–b, show that during the energy conversion there is an increase in the IPSD in the ULF band close to or superimposed on these regions, being able to interact effectively with particles that cross there.

The interval *I*4 represents the region of the MC-type structure, see Figure 2e, where the B_z component is mostly southward directed, with mean value ∼−18.4 nT, and the B_y component oscillates around zero. The magnetopause position oscillated around a typical value of 10 R_E, and the average solar wind velocity component V_x ∼ 368 km/s. In Figure 12, the upper row illustrates the color maps of the medians of the energy conversion terms.

This interval, *I*4, which started at 02:27 UT on the 28th of May, was selected because it was within the main phase of the magnetic storm. Also, a substorm occurred on this day, as it can be seen in both the SYM–H and A_E profiles in Figures A1e and A1f. During the storm's main phase the physical process of magnetic reconnection is in high activity on the dayside of the magnetopause. The power is carried by electric and magnetic fields, as probed by the ϵ parameter was ∼1.5×10^{12} W. We can see by the median of the energy conversion terms that there is a high activity in the IM of energy conversion, it is noted that the most accentuated exchange between magnetic and internal energy. We can also see that there is an increase in ULF wave activity as observed by the Van Allen Probes (see Section 3).

We can observe in Figure 12, top row, the median of the color map, high activity in energy conversion being established in response to the change in the orientation of the B_z. Two large spatial extensions, in both energy conversion components, can be observed in the 15:00 LT—19:00 LT range on the dusk side and at midnight 00:00 LT through 11:00 LT on the dayside. We observe a dynamo region forming (red color, in the color map of the E_m) by the exchange between internal and kinetic energy. We also note that the exchange regions between magnetic and internal are of greater extension than the kinetic, where the latter participation is more evident on both flanks. The most evident and intense response in the IPSD of the poloidal and toroidal components was the toroidal component, with intensification regions close to or superimposed on the energy conversion region.

The *I*5 interval illustrates the region of MC-like interplanetary structure, which interacts with the global and IM Figure 2e. During this period, the position of the subsolar magnetopause oscillates around ∼9.8 R_e, the IMF components B_z and B_y have very similar mean values ∼−9.7 and −9.9 nT respectively. The dynamic pressure

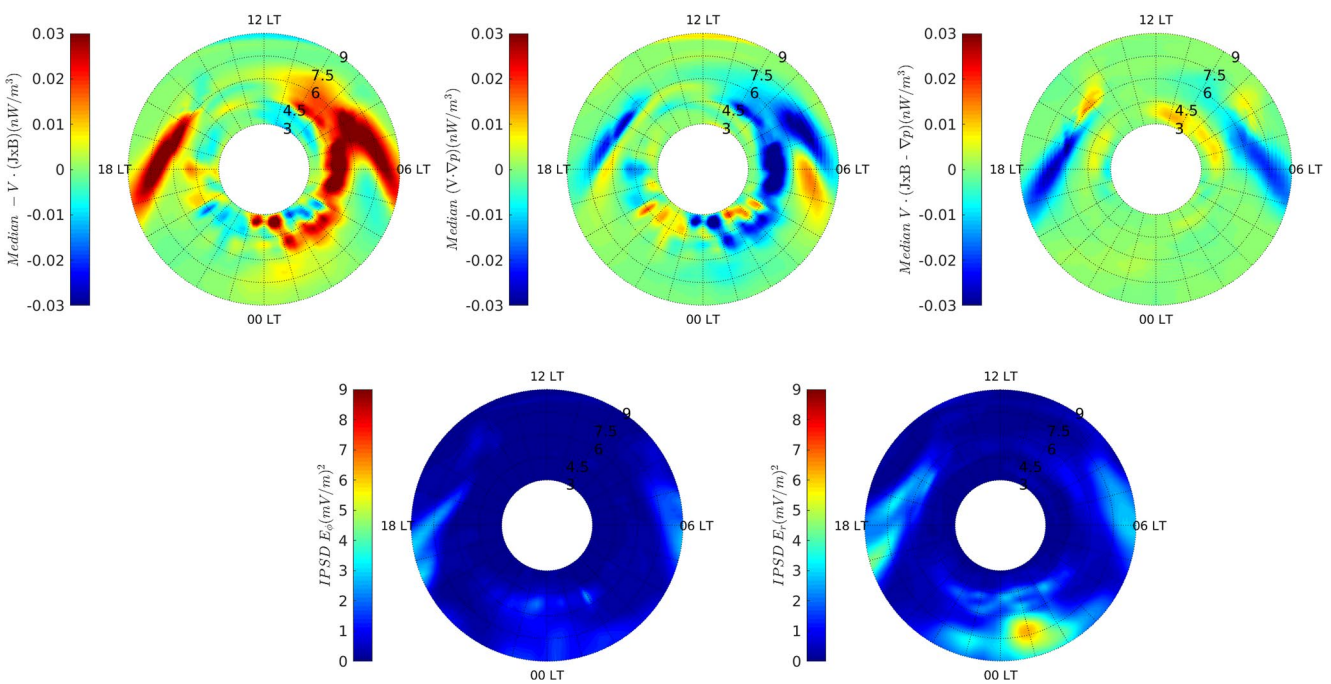

Figure 12. Shows the *I*4 interval. The first row above left to right represents the median of the magnetic energy conversion term, the second represents the internal energy conversion term, and the last term represents the kinetic energy conversion. The second row represents the integrated power spectral density of the azimuthal and radial electric field component in the equatorial plane at $z = 0$. Both the median and the integrated values were taken within 2 hr.

of the solar wind is around ∼2 nPa and the speed of the solar wind oscillates on average around 355 km/s. The average power transferred via ϵ is $\sim 1.0 \times 10^{12}$W, a value close to that shown in the previous interval *I*4. In this interval, the internal and GM continues at a high level of energy conversion, however, it is already moving to the recovery phase as shown in the Figures A1e and A1f.

In the color map of the energy conversion components Figure 13 the energy conversion/transfer pattern is similar to the interval *I*4. We can see that the energy conversion is happening more intensely between the magnetic and internal components, with the mediation of kinetic energy that occurs mainly in the flanks region. As discussed in the article by Tanaka (2007) and verified in our study, the kinetic energy conversion term in the internal magnetosphere presented itself as having the lowest value in relation to the other two energy conversion terms. However, the kinetic energy transfer term is always present mediating the process. In Figure 13, the magnetic and internal energy conversion region has large spatial dimensions with greater intensity in the night-to-dayside transition starting at LT 4:00 at outermost radial distances and extending to the dayside region at innermost radial distances. We also note that for inner radial distances, that is, $R < 5\ R_E$, the energy conversion pattern shows oscillatory behavior. The IPSD response from the radial and azimuthal components, also shares these regions, with greater intensity being observed in the radial component.

The last analyzed interval corresponds to *I*6, which represents the MC region, with a marked change in the orientation of the IMF component. The average value of the positive B_z component over the 2-hr long interval was ∼0.7 nT. The predominant IMF component in this interval was B_y oscillating with an average value of −13 nT, which is essentially an intense dawnward component of the IMF. The v_x component of the solar wind remains oscillating around 355 km/s, similar to the *I*5 interval. The dynamic pressure of the solar wind also remains oscillating around values representative of the quiet solar wind ∼2.2 nPa. The mean position of the subsolar magnetopause oscillated around $10R_E$. The average power carried by the solar wind through the ϵ was $\sim 1.61 \times 10^{11}$ W, within the order of magnitude observed for the interval *I*3.

In the color map of Figure 14 in the first row we can see some interesting characteristics in the conversion of magnetic, thermal, and kinetic energy and also in the integrated power of the poloidal and toroidal components of the electric field. The energy conversion decreases appreciably compared to the ranges *I*2, *I*3, *I*4, and *I*5. We found that the spatial pattern of energy conversion is similar to the *I*4 and *I*5 intervals, however with an asymmetry

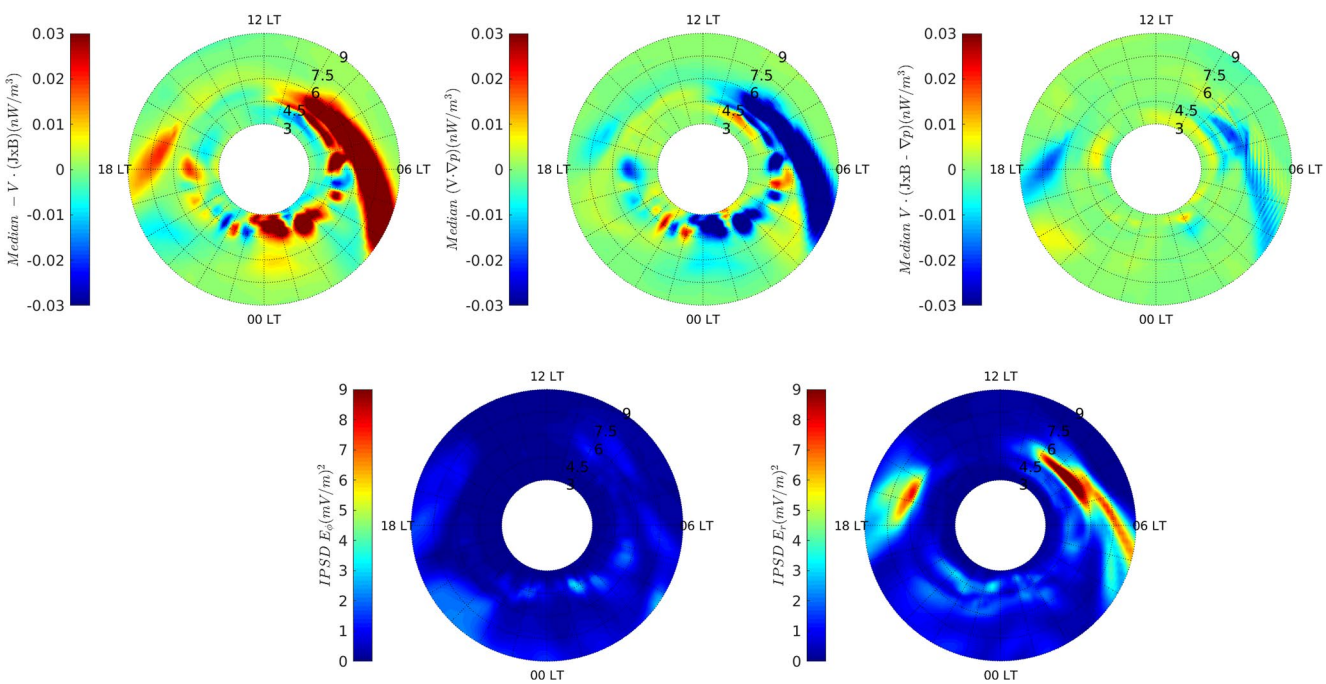

Figure 13. Represents the *I*5 interval. The first row above left to right represents the median of the magnetic energy conversion term, the second represents the internal energy conversion term and the last term represents the kinetic energy conversion. The second row represents the integrated power spectral density for the radial and azimuthal component of the electric field component in the equatorial plane at $z = 0$. Both the median and the integrated values were taken within 2 hr.

tending to intensify the energy conversion toward the dawnside, as already observed in the *I*4 and *I*5 intervals. The energy conversion rate is mainly between magnetic and internal, with low intensity mediated by kinetic energy. We observed that the energy conversion is concentrated for more inner regions $R < 6$, with the exception of the dawnside region, and the conversion is predominant between internal and magnetic. The power of the ULF waves for the poloidal component has a peak around the LT ~ 3:00 and $R \sim 6$ predominant in the nightside region. The IPSD of the toroidal component follows the pattern of energy conversion, both in the dayside and at nightside. It has a power distributed around 18:00–00:00 LT for the nightside region and a power increase region from 06:00–12:00 LT in the dayside sector region. If we compare the IPSD color maps of the poloidal and toroidal components, from the *I*5 to the *I*6 interval, it appears that the intensification of the dawnward IMF component caused the power to have a sector-centered shift (18:00–00:00) nightside LT and sector (6:00–12:00) LT dayside region. What we can observe is that the major effect of the B_y component, and still maintain the energy conversion both in the dayside and nightside regions, however for more inner radial distances $R < 6\ R_E$, that is, closer to Earth. The asymmetry observed in the energy conversion tending toward the dawn sector is strongly correlated with the physics modeled by the RCM component, due to the internal dynamics during the storm and substorm period. The details of this intense asymmetry have already been discussed in Jauer et al. (2019).

We can see from the analysis and discussions conducted above that the event between the 27th and 29th of May 2017 had an intense and abrupt impact on both the global and IM. Through global MHD modeling, with real solar wind parameters, we obtained a global view of the magnetosphere response in terms of energy conversion and the emergence and intensification of the poloidal and toroidal electric field oscillation modes in the equatorial plane ($z = 0$).

In general, we can associate which energy conversion region can be connected with the increase and intensification of the IPSD of both electric field components. This study found that the toroidal component had a more intense response. MHD wave dispersion relation is proportional to the ambient magnetic field magnitude squared and plasma density ratio. Therefore, the magnetic energy stored in the magnetic field acts to cause tension over the field lines and promotes two normal oscillation modes, poloidal and toroidal (Dungey, 1967; Kivelson & Russell, 1995). The initial conditions of the plasma disturbance can favor one specific mode, although a combination of them is expected when the system gains energy by some conversion process. The energy conversion

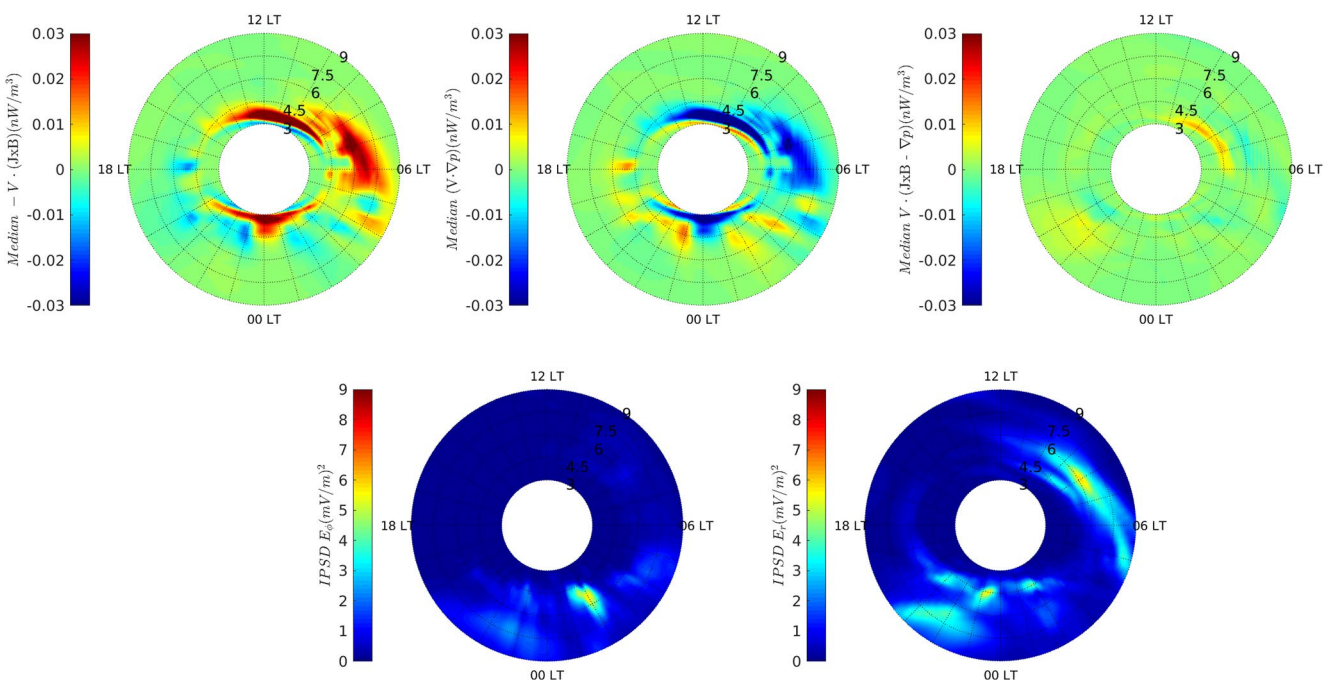

Figure 14. Represents the *I*6 interval. The first row above left to right represents the median of the magnetic energy conversion term, the second represents the internal energy conversion term and the last term represents the kinetic energy conversion. The second row represents the integrated power spectral density for the radial and azimuthal component of the electric field component in the equatorial plane at $z = 0$. Both the median and the integrated values were taken within 2 hr.

process in physical systems is not fully efficient; the energy excess is often released into waves in the ambient. In the magnetosphere, magnetic energy surplus from the conversion in internal or kinetic terms is related to the increase of ULF PSD, as shown in the bottom panels in Figures 8–14. Accordingly, the results show that the regions where energy conversion rates (ECRs) are higher correlate to those where high ULF PSD is observed. Therefore, the magnetic energy conversion excess provides energy to ULF waves, and this process might be initiated when the conversion surpasses a given threshold. Figures 8–14 show that in the intervals *I*3 to *I*6, the magnetic energy term gains energy from the other (internal and kinetic) terms, except for *I*2, when the magnetic term loses significant energy to the kinetic term. As the magnetic energy for MHD waves is stored in the magnetic field, ULF waves are expected to result from any energy changes related to the magnetic field term, even if they lose energy, as shown in Figure 8.

The energy stored in the ULF waves can be supplied to the particles increasing their energy as they cross these regions. As discussed above, the toroidal component, in general, had a more significant intensification due to the abrupt coupling of the structure favored the intensification of this toroidal mode, which may also be necessary for particle acceleration in the radiation belts region (Elkington et al., 2004). The effect of this toroidal component disappears in regions where the magnetic field presents symmetry, that is, for more internal regions. In addition to our results regarding ECRs and the disturbances in the frequency range of the ULF waves, we must also take into account the fact that during this period the magnetosphere was under the action of an intense and prolonged B_z southward that can promote the physical process of magnetic reconnection in the magnetopause and also later with the accumulation of magnetic flux in the region of the magnetic tail, in particular in the current sheet (Dungey, 1967; Gonzalez et al., 1994). The magnetic reconnection at nightside region can promote an abrupt and localized release of energy accumulated in the magnetic field in the form of Bursty bulk flows (BBFs) (Angelopoulos et al., 1994; Baumjohann et al., 1990; Zhang et al., 2010, 2020). These mesoscale structures of fast flow may be associated during periods of storms and substorms by transporting mass, momentum, and energy (Angelopoulos et al., 1994; Keesee et al., 2021; Wiltberger et al., 2015) and also by wave activity in the IM (Wang et al., 2020). In addition to observational study of these fast flows, numerical simulations were carried out specially configured to capture and better understand and describe the dynamics and consequently the better characterization of these BBF structures that can continuously affect the global magnetosphere and the ionosphere (Cramer et al., 2017; Keesee et al., 2021; Wiltberger et al., 2015).

In this way, and attempting to understand better the cause and effects in the results already shown, we tried to look for evidence of these fast structures in our simulation results and compare them with observational data during the analyzed period. To perform this verification on our modeled results, we extract temporal profiles of the magnetic field, velocity, thermal pressure, and density Figure B1 along the orbit of MMS1(Burch et al., 2015) and compare with the observed magnetic field from fluxgate magnetometers(Russell et al., 2014), density and bulk velocity from the fast plasma investigation (FPI) (Pollock et al., 2016) from MMS1 Figure B2. The interval analyzed started at 12:00 on 27 May until 29 May at 00:30. The starting position of MMS-1 was $(-10.17, -1.66, -0.04)\ R_E$ and the ending position $(-17.35, -16.89, -0.08)\ R_E$, the location remained most of the time in the post-midnight sector. To verify the possible occurrence of BBF-like structures in our modeled results in Figure B1 of the Appendix B, we followed the criterion given by Angelopoulos et al. (1994); Schödel et al. (2001) where the component $V_x \geq 400$ km/s and $|\vec{V} \times \vec{B}| \geq 2$ mV/m, however there may be additional features due to the physical nature of the phenomenon such as reduced density and plasma pressure (Johansson et al., 2009). Following the criteria, we can find evidence in our results of the presence of these BBF structures mostly during the period of greater coupling of the interplanetary structure. In the Figure B1, shows a vertical black line at 00:26 UT on 28 May where the component V_x has a peak of 522 km/s, illustrated in the second panel. The third panel shows an abrupt decrease in plasma thermal pressure, in the fourth panel a peak in the electric field modulus above 2 mV/m is also observed and in the last panel a decrease in plasma density. We can also see an increase in the B_z and B_y component of magnetic field first panel in red and green color respectively. All these features fit the description of BBF signature and are recurrent in the other time intervals, for example, around 04:15 UT illustrated by the vertical black line which in general agrees with the data observed by MMS1 Figure B2. It may be possible that these BBF-like structures when approaching and interact with Earth's magnetosphere in the nightside region are mediating the energy conversion and possible dynamics of the ULF waves, however, these are only speculations. Unfortunately our spatial grid configuration used may not be refined enough to solve in detail these BBF-like structures compared to the simulations already carried out (Cramer et al., 2017; Keesee et al., 2021; Wiltberger et al., 2015), thus, a point-to-point comparison with the observations loses the sense of validity. In the future,

we intend to perform simulation with configurations that allow an adequate capture of BBF, including non-ideal effects in the MHD model.

Borovsky and Denton (2006), listed 21 differences between CME-driven geomagnetic storms and CIR-driven geomagnetic storms. One of the main effects of the interaction of the CME-like structure is an increase in the RC. Its effects are short-lived and abrupt, which can potentially affect the magnetospheric environment through the intensification of the GICs. The CIRs, including the fast solar wind, are structures that affect the magnetosphere for a long period due to the solar characteristics (27-day rotation). They are more effective in accelerating electrons to relativistic speeds that can damage electronic devices onboard satellites. The time interval of ULF wave activity, for example, due to the interaction of a CME-type structure is shorter than the persistent ULF wave activity due to the interaction of a CIR-type recurrent interplanetary structure. Some fundamental physical questions remain open about the impact of each of the structures mentioned above on the dynamics of the relativistic electrons that populate the inner magnetosphere. What are the physical processes behind each interaction that would favor this complex dynamic? For more details on open physical issues (see, e.g., Fok et al., 2014; Borovsky & Denton, 2006).

6. Summary and Conclusion

In this research, we modeled the interaction of a geoeffective interplanetary structure (magnetic cloud) that occurred between 27–29 May, 2017, giving rise to an intense storm with SYM-H < -100 nT and high activity in the auroral region measured by the AE index that had peaked around 2000 nT.

The modeling of this MC-like interplanetary structure lasted 46 hr, capturing all the dynamics involving the interaction of this structure with the global and IM in terms of energy conversion/transfer and fluctuations in the frequency range of the ULF waves. To carry out a detailed analysis, we separated the entire period analyzed into seven key intervals, of 2 hours long, where we performed the analysis of the spatial distribution of energy conversion through color maps of the medians and the integrated power (IPSD) of the poloidal and toroidal components of the electric field.

The main results can be summarized as follows:

- During the intervals *I*1 and *I*7, the IM showed a low activity level. The interval *I*1 represented the quiet interplanetary medium before the interaction, and a persistent northward IMF B_z characterized the interval *I*7 (not shown).
- The intervals *I*2 and *I*3 present similar behavior in terms of the spatial distribution of energy conversion. During interval *I*2, the magnetosphere is strongly compressed due to the high dynamic pressure value. As a result, the toroidal component of the electric field in the dayside and nightside region is more active than the poloidal one. We can identify the magnetopause region compressed within the study domain for both IPSD and the color map of the median energy conversion. The inner dynamics in terms of energy conversion and increase in IPSD were mostly due to the intense compression period as the main phase of magnetic storm and substorm was not yet developing. The *I*3 interval had a very intense response in the nightside region both in the IPSD and energy exchange.
- The intervals *I*4 and *I*5 present a similar spatial distribution of energy conversion and intensification of ULF waves in the toroidal and poloidal components. The toroidal component was the most active, with peaks at dusk (18 LT) and dawn (06 LT) and in the region at 00 LT. However, similar regions were activated in the poloidal component with its lower intensity. Concerning the observations, we observed that the Interval *I*4 had the highest peak of activity of ULF waves in the poloidal component. In the simulation, we observed a greater intensification of the toroidal component during the *I*3, *I*4 and *I*5 intervals. Where intervals *I*4 and *I*5 are within storm and substorm development. During intervals *I*4 and *I*5 the energy conversion region becomes extremely activated and extends to greater radial distances. The predominant conversion components are internal and magnetic energy, where kinetic energy is predominantly active on the flanks of the equatorial magnetosphere. A large region of dynamos is established.
- As shown in Figures 9a and 9b and also verified in the other intervals, the energy conversion region either closes or overlaps the enhancements of the poloidal and toroidal components, more evident in the toroidal component. As already reported by Tanaka (2007), the largest source of energy in the interplanetary medium is contained in the kinetic component. However, when we change the scenario, we are going to

analyze within the magnetosphere the two components that the strongest exchange of energy is between the magnetic and internal. In this study, we observed for this event, mostly the exchange or conversion takes place between the magnetic and thermal energies, however, the kinetic energy is always present, mediating the process.

- In the interval *I*6, which is during the storm recovery phase and coincidentally with the magnetic cloud phase with intense IMF B_y dawnward. We observed that the energy conversion rate remained active and concentrated on radial distances $R < 6\ R_E$, in most equatorial planes, except in the dawn region, maintaining the asymmetry seen in the intervals *I*4 and *I*5, however with reduced intensity. The kinetic energy conversion component becomes extremely low over much of the equatorial plane oscillating around zero. We observed that the toroidal component of the electric field is mostly active in the regions 20:00–02:00 LT and 05:00–10:00 LT. The poloidal component of the field is active in the nightside region at ∼LT 02:00 around $R \sim 6$. If we compare with the interval *I*5 and *I*6, a displacement occurred in the regions of IPSD's. Again, we observe that the conversion regions are close to or overlap the IPSD increase regions.
- We found evidence in the results modeled and observed by MMS-1 of the occurrence of BBF's that may be associated with the energy conversion rate in the IM and the respective increase or decrease in the power of the ULF waves.

In view of the open physical questions mentioned at the end of the Section 5, we intend to carry out future controlled numerical experiments. These numerical experiments would select the main characteristics of the plasma that characterize CME and CIR structures that can be geoeffective and promote the emergence of storms, substorms, and the intensification of the spectral power of waves in the internal and GM. These numerical experiments could answer some important physical questions. For example, during a CIR event, the energy conversion between E_m, E_i, and E_k is predominant in which components? If the poloidal component is intensified during the CIR event relative to the CME, which energy conversion component has the greatest contribution and why?

Appendix A: Mean Interplanetary Plasma Parameters and Geomagnetic Indices

The mean values for both solar wind and magnetospheric activity parameters for each of the seven 2-hr long intervals presented in Figure A1 are shown in Table A1. The first column in Table A1 shows the physical quantities that characterize the interplanetary structure, that are: the magnitude, By and Bz component of the magnetic field, the dynamic pressure of the solar wind, the magnitude of the velocity, the position of the magnetopause, the energy dissipation and the density of the solar wind. Columns 2 to 8 represent the mean values of the physical quantities for each two-hour long interval. In Figure A1, panels A and B show the time series of the By and Bz components of the interplanetary magnetic field. In panel C illustrates the

Table A1
Each Column Identified With the I's Represents the Average Values Within the 2 hr Long Intervals

	*I*1	*I*2	*I*3	*I*4	*I*5	*I*6	*I*7
$\|B\|$ (nT)	3.01	4.36	15.25	19.65	16.23	16.97	13.41
B_y (nT)	−2.02	0.9813	8.03	0.39	−9.93	−13.37	0.84
B_z (nT)	−1.04	−0.56	−7.82	−18.41	−9.76	0.76	11.69
Pdyn (nPa)	1.01	16.35	14.66	2.14	2.84	2.20	2.45
$\|v\|$ (km/s)	304.0	375.7	366.6	369.1	356.2	357.7	341.3
Mp (R_e)	11.36	7.46	7.64	10.15	9.79	10.12	9.94
ϵ (*W*) ($\times 10^{10}$)	1.98	6.05	68.3	153	103	16.1	5.71
N (#/cm^3)	5.58	58.99	55.37	8.02	11.43	8.78	10.76

Note. The first column in the second row represents the average value of the IMF modulus. The third and fourth rows represent the mean values of the B_y and B_z components of the IMF, respectively. In the fifth row the mean value of the dynamic pressure of the solar wind is shown. The average value of the velocity modulus is shown in the sixth row. The average position of the calculated magnetopause is shown in the seventh row. The average value of power dissipated for each interval I's is illustrated in the eighth row. in the last row the average density value is illustrated in each of the I's intervals. Each of the plasma parameters illustrated in the table characterize the average intensity of the MC type event

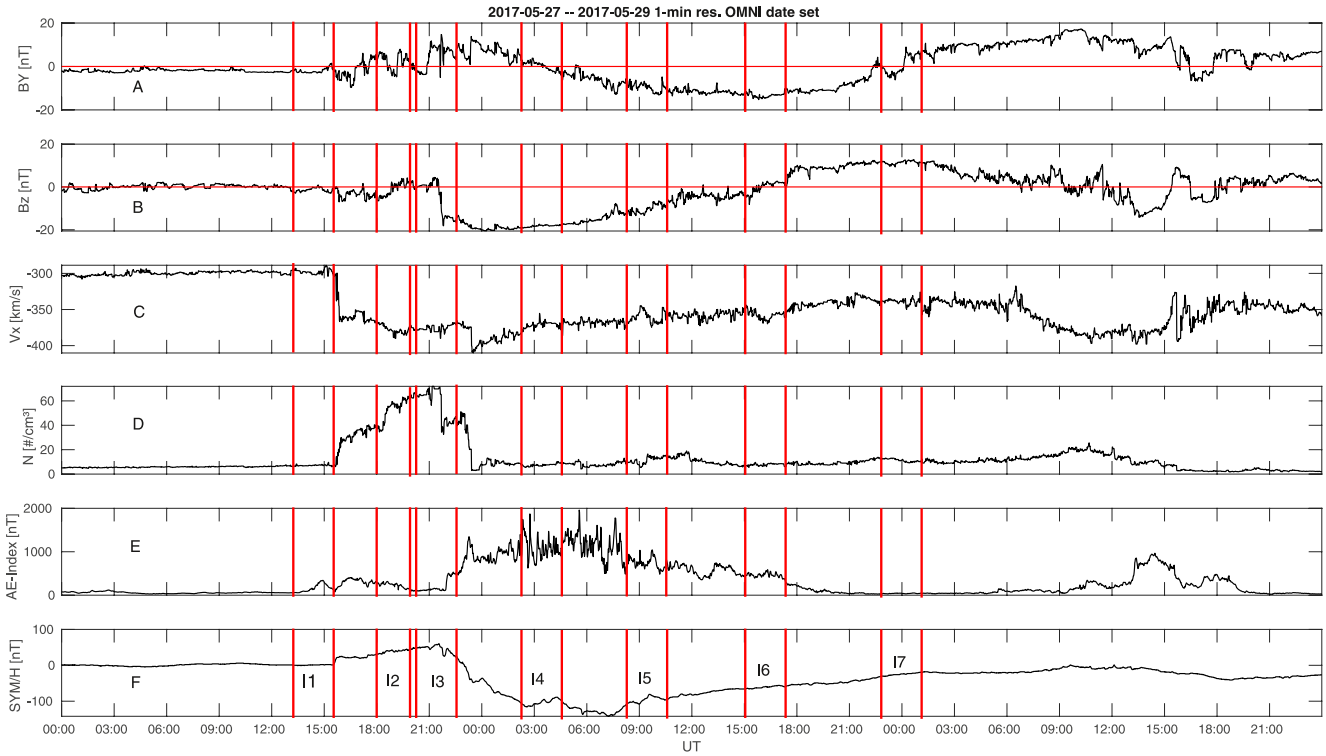

Figure A1. Shows solar wind plasma parameters *AE* and *SYM*-H magnetospheric indices. The vertical red lines represent each 2 hr long I's interval. Panels (a–d) illustrate the B_y, B_z, V_x and the solar wind density respectively. Panels (e, f) show the *AE* and *SYM-H* indices that illustrate the activity level of the inner magnetosphere. The data obtained in: https://omniweb.gsfc.nasa.gov/form/omni_min.html.

Vx component of the solar wind speed. In panel D the density of the solar wind is shown. In panels E and F illustrate the AE and SYM-H index, which measure the level of disturbance in the inner magnetosphere. The vertical lines in red color illustrate the two-hour long intervals from I1 to I7 where the analyzes were performed.

Appendix B: Comparison Between Observational and Modeled Data in the MMS-1 Orbit

Panel A in Figure B1 shows the three components of the magnetic field and its modeled magnitude. In panel B, the three components of plasma velocity are shown. The horizontal black line is fixed at 400 km/s. In panel C the plasma pressure is illustrated. In panel D the three components of the convection electric field, together with their magnitude, are shown. The horizontal blue line is fixed at 2mV/m in panel D. In panel E the plasma density is illustrated during the analyzed interval. Panel A in Figure B2 illustrates the time series of observational data of the three components of the velocity along the MMS-1 orbit. The horizontal blue line is fixed at 400 km/s. In panel B shows the observational profiles of the three components of the magnetic field and its magnitude along the orbit of MMS-1. In panel C the three components of the convection electric field and its magnitude are shown. The horizontal blue line is fixed at 2 mV/m. In panel D the plasma density along the MMS-1 orbit is illustrated during the analyzed period.

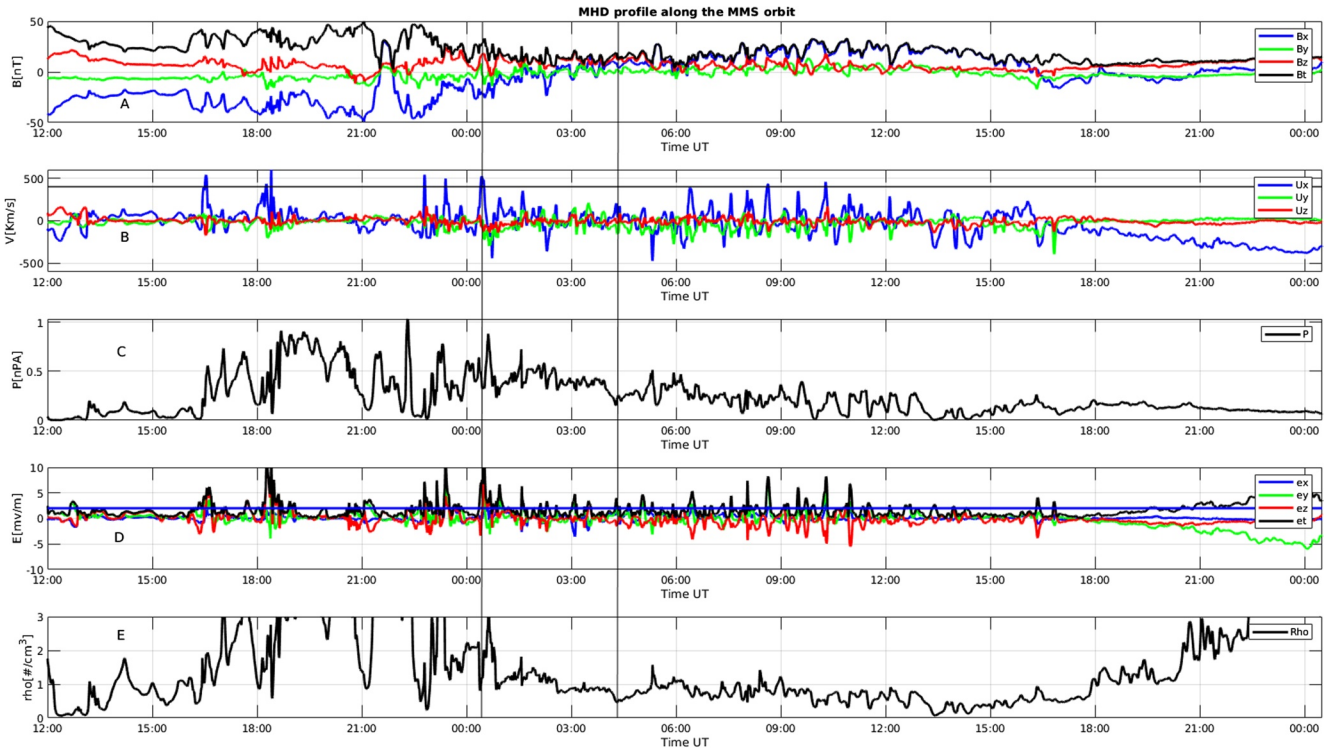

Figure B1. Shows the modeled plasma parameters extracted along the orbit of the MMS-1 satellite starting on 27 May at 12:00 a.m. and ending at 00:30 on 29 May. The first panel A represents the three components of the magnetic field B_x, B_y, and B_z together with the modulus of B. The second panel (b) illustrates the three components of the velocity V_x, V_y and V_z. The plasma thermal pressure P is shown in panel (c) Panel (d) shows the total convection electric field and its three components E_x, E_y, and E_z. The horizontal blue line is fixed at 2 mV/m. The last panel E represents protons density during the analyzed period. The starting position of MMS-1 was x_i, y_i, $z_i = (-10.17, -1.66, -0.04)$ R_E and the ending position x_f, y_f, $z_f = (-17.35, -16.89, -0.08)$ R_E your location remained most of the time in post-midnight sector.

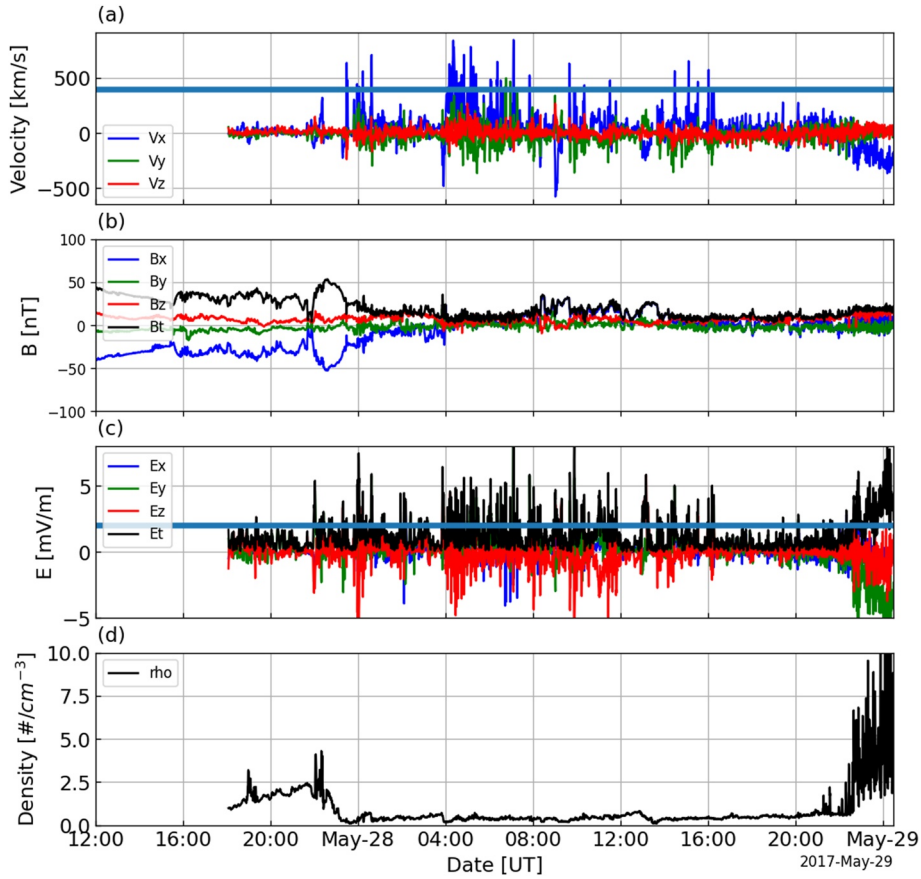

Figure B2. Shows the plasma parameters extracted along the orbit of the MMS-1 satellite starting on 27 May at 12:00 a.m. and ending at 00:30 on 29 May. The first panel (a) illustrates the three components of the velocity V_x, V_y, and V_z (Pollock et al., 2016). The second panel (b) represents the three components of the magnetic field B_x, B_y, and B_z together with the modulus of B (Russell et al., 2014). Panel (c) shows the total convection electric field E_t and its three components E_x, E_y and E_z. The last panel (d) represents protons density during the analyzed period. The starting position of MMS-1 was x_i, y_i, $z_i = (-10.17, -1.66, -0.04)$ R_E and the ending position x_f, y_f, $z_f = (-17.35, -16.89, -0.08)$ R_E your location remained most of the time in post-midnight sector.

Data Availability Statement

Data used in this research are available at:

- DSCOVR: https://ccmc.gsfc.nasa.gov/requests/GetInput/get_dscovr_L2.php
- EMFISIS: https://emfisis.physics.uiowa.edu/Flight/
- EFW: https://cdaweb.gsfc.nasa.gov/pub/data/rbsp/
- AE Index: https://cdaweb.gsfc.nasa.gov/pub/data/omni/
- SYM/H index: https://cdaweb.gsfc.nasa.gov/pub/data/omni/.

References

Akasofu, S.-I. (1981). Energy coupling between the solar wind and the magnetosphere. *Space Science Reviews*, *28*(2), 121–190. https://doi.org/10.1007/bf00218810

Alves, M., Echer, E., & Gonzalez, W. (2006). Geoeffectiveness of corotating interaction regions as measured by Dst index. *Journal of Geophysical Research: Space Physics*, *111*(A7), A07S05. https://doi.org/10.1029/2005JA011379

Angelopoulos, V., Kennel, C. F., Coroniti, F. V., Pellat, R., Kivelson, M. G., Walker, R. J., et al. (1994). Statistical characteristics of bursty bulk flow events. *Journal of Geophysical Research*, *99*(A11), 21257–21280. https://doi.org/10.1029/94JA01263

Baker, D. (2021). Wave–particle interaction effects in the Van Allen belts. *Earth Planets and Space*, *73*(1), 1–13. https://doi.org/10.1186/s40623-021-01508-y

Baker, D., Kanekal, S., Li, X., Monk, S., Goldstein, J., & Burch, J. (2004). An extreme distortion of the Van Allen belt arising from the 'Hallowe'en'solar storm in 2003. *Nature*, *432*(7019), 878–881. https://doi.org/10.1038/nature03116

Acknowledgments
This work was carried out using the SWMF/BATSRUS tools developed at the University of Michigan Center for Space Environment Modeling (CSEM) and made available through the NASA Community Coordinated Modeling Center (CCMC). The authors would like to thank the developers of the MHD model. P.R.J., L.A.S., J.P.M and D. S. would like to thank the financial support from China-Brazil Joint Laboratory for Space Weather. This research was also supported by the International Partnership Program of the Chinese Academy of Sciences (183311KYSB20200003 and 183311KYSB20200017). The authors thank MCTI/FINEP (CT-INFRA Grant 0112052700) and the EMBRACE Space Weather Program for the computing facilities at INPE where the SWMF/BATSRUS code was run. Data at the L1 Lagrangian point provided by the ACE spacecraft can be readily found at http://www.srl.caltech.edu/ACE/ASC/level2/index.html. E. Echer would like to thank Brazilian agencies for research Grants CNPq/PQ (201883/2019-0) and FAPESP (2018/21657-1). Souza acknowledges support from the Brazilian National Council for Scientific and Technological Development (CNPq) PCI Grant (300342/2022-5). L.E.A.V would like to thank Brazilian Space Agency (AEB) for the funding (004/2020-AEB/PO20VB.0009) and CNPq/MCTIC Grant (308355/2020-2). L.R. Alves thanks for financial support by CNPq through PQ-Grant (309026/2021-0).

Baker, D. N., & Daglis, I. A. (2007). Radiation belts and ring current. In *Space weather-physics and effects* (pp. 173–202). Springer. https://doi.org/10.1007/978-3-540-34578-7_6

Baker, D. N., Mason, G. M., Figueroa, O., Colon, G., Watzin, J. G., & Aleman, R. M. (1993). An overview of the solar anomalous, and magnetospheric particle explorer (SAMPEX) mission. *IEEE Transactions on Geoscience and Remote Sensing*, *31*(3), 531–541. https://doi.org/10.1109/36.225519

Baumjohann, W., Paschmann, G., & Lühr, H. (1990). Characteristics of high-speed ion flows in the plasma sheet. *Journal of Geophysical Research*, *95*(A4), 3801–3809. https://doi.org/10.1029/JA095iA04p03801

Birn, J., & Hesse, M. (2005). Energy release and conversion by reconnection in the magnetotail. *Annales Geophysicae*, *23*(10), 3365–3373. https://doi.org/10.5194/angeo-23-3365-2005

Borovsky, J. E., & Denton, M. H. (2006). Differences between CME-driven storms and CIR-driven storms. *Journal of Geophysical Research*, *111*(A7), A07S08. https://doi.org/10.1029/2005JA011447

Brenner, A., Pulkkinen, T. I., Al Shidi, Q., & Toth, G. (2021). Stormtime energetics: Energy transport across the magnetopause in a global MHD simulation. *Frontiers in Astronomy and Space Sciences*, *180*, 16. https://doi.org/10.3389/fspas.2021.756732

Burch, J. L., Moore, T. E., Torbert, R. B., & Giles, B. L. (2015). Magnetospheric multiscale overview and science objectives. *Space Science Reviews*, *199*(1–4), 5–21. https://doi.org/10.1007/s11214-015-0164-9

Burlaga, L., Fitzenreiter, R., Lepping, R., Ogilvie, K., Szabo, A., Lazarus, A., et al. (1998). A magnetic cloud containing prominence material: January 1997. *Journal of Geophysical Research*, *103*(A1), 277–285. https://doi.org/10.1029/97JA02768

Burlaga, L. F., & Burlaga, L. F. (1995). *Interplanetary magnetohydrodynamics*. Oxford University Press on Demand.

Carrington, R. C. (1859). Description of a singular appearance seen in the sun on September 1, 1859. *Monthly Notices of the Royal Astronomical Society*, *20*(1), 13–15. https://doi.org/10.1093/mnras/20.1.13

Chapman, S., & Ferraro, V. C. (1933). A new theory of magnetic storms. *Terrestrial Magnetism and Atmospheric Electricity*, *38*(2), 79–96. https://doi.org/10.1029/TE038i002p00079

Claudepierre, S., Elkington, S., & Wiltberger, M. (2008). Solar wind driving of magnetospheric ULF waves: Pulsations driven by velocity shear at the magnetopause. *Journal of Geophysical Research*, *113*(A5), 19363–19372. https://doi.org/10.1029/2007JA012890

Claudepierre, S., Hudson, M., Lotko, W., Lyon, J., & Denton, R. (2010). Solar wind driving of magnetospheric ULF waves: Field line resonances driven by dynamic pressure fluctuations. *Journal of Geophysical Research*, *115*(A11), A11202. https://doi.org/10.1029/2010JA015399

Cramer, W. D., Raeder, J., Toffoletto, F. R., Gilson, M., & Hu, B. (2017). Plasma sheet injections into the inner magnetosphere: Two-way coupled OpenGGCM-RCM model results. *Journal of Geophysical Research: Space Physics*, *122*(5), 5077–5091. https://doi.org/10.1002/2017JA024104

Da Silva, L. A., Shi, J., Alves, L. R., Sibeck, D., Marchezi, J. P., Medeiros, C., et al. (2021). High-energy electron flux enhancement pattern in the outer radiation belt in response to the Alfvénic fluctuations within high-speed solar wind stream: A statistical analysis. *Journal of Geophysical Research: Space Physics*, *126*(8), e2021JA029363. https://doi.org/10.1029/2021JA029363

Da Silva, L. A., Shi, J., Alves, L. R., Sibeck, D., Souza, V. M., Marchezi, J. P., et al. (2021). Dynamic mechanisms Associated with high-energy electron flux Dropout in the Earth's outer radiation belt under the influence of a coronal mass ejection sheath region. *Journal of Geophysical Research: Space Physics*, *126*(1), 1–30. https://doi.org/10.1029/2020JA028492

Da Silva, L. A., Sibeck, D., Alves, L. R., Souza, V. M., Jauer, P. R., Claudepierre, S. G., et al. (2019). Contribution of ULF wave Activity to the global recovery of the outer radiation belt during the passage of a high-speed solar wind stream observed in september 2014. *Journal of Geophysical Research: Space Physics*, *124*(3), 1660–1678. https://doi.org/10.1029/2018JA026184

De Zeeuw, D. L., Sazykin, S., Wolf, R. A., Gombosi, T. I., Ridley, A. J., & Tóth, G. (2004). Coupling of a global MHD code and an inner magnetospheric model: Initial results. *Journal of Geophysical Research*, *109*(A12), A12219. https://doi.org/10.1029/2003JA010366

Dungey, J. W. (1961). Interplanetary magnetic field and the auroral zones. *Physical Review Letters*, *6*(2), 47–48. https://doi.org/10.1103/PhysRevLett.6.47

Dungey, J. W. (1967). Hydromagnetic waves. In S. Matsushita & W. H. Campbell (Eds.), *Physics of geomagnetic phenomena* (p. 913). Academic Press.

Ebihara, Y., Fok, M.-C., Sazykin, S., Thomsen, M. F., Hairston, M. R., Evans, D. S., et al. (2005). Ring current and the magnetosphere-ionosphere coupling during the superstorm of 20 November 2003. *Journal of Geophysical Research: Space Physics*, *110*(A9). https://doi.org/10.1029/2004JA010924

Ebihara, Y., & Tanaka, T. (2017). Energy flow exciting field-aligned current at substorm expansion onset. *Journal of Geophysical Research: Space Physics*, *122*(12), 12288–12309. https://doi.org/10.1002/2017JA024294

Ebihara, Y., & Tanaka, T. (2020). Evolution of auroral substorm as viewed from MHD simulations: Dynamics, energy transfer and energy conversion. *Reviews of Modern Plasma Physics*, *4*(1), 1–29. https://doi.org/10.1007/s41614-019-0037-x

Elkington, S. R. (2006). A review of ULF interactions with radiation belt electrons. *Magnetospheric ULF waves: Synthesis and new directions*, *169*, 177–193. https://doi.org/10.1029/169GM12

Elkington, S. R., Hudson, M. K., & Chan, A. A. (1999). Acceleration of relativistic electrons via drift-resonant interaction with toroidal-mode Pc-5 ULF oscillations. *Geophysical Research Letters*, *26*(21), 3273–3276. https://doi.org/10.1029/1999GL003659

Elkington, S. R., Wiltberger, M., Chan, A. A., & Baker, D. N. (2004). Physical models of the geospace radiation environment. *Journal of Atmospheric and Solar-Terrestrial Physics*, *66*(15–16), 1371–1387. https://doi.org/10.1016/j.jastp.2004.03.023

Fok, M.-C., Buzulukova, N., Chen, S.-H., Glocer, A., Nagai, T., Valek, P., & Perez, J. (2014). The comprehensive inner magnetosphere-ionosphere model. *Journal of Geophysical Research: Space Physics*, *119*(9), 7522–7540. https://doi.org/10.1002/2014JA020239

Friedel, R., Reeves, G., & Obara, T. (2002). Relativistic electron dynamics in the inner magnetosphere—A review. *Journal of Atmospheric and Solar-Terrestrial Physics*, *64*(2), 265–282. https://doi.org/10.1016/S1364-6826(01)00088-8

Goldstein, H. (1983). On the field configuration in magnetic clouds. In M. Neugebauer (Ed.), *JPL solar wind five* (Vol. 228). NASA. Retrieved from http://hdl.handle.net/2060/19840005057

Gombosi, T. I., Chen, Y., Glocer, A., Huang, Z., Jia, X., Liemohn, M. W., et al. (2021). What sustained multi-disciplinary research can achieve: The space weather modeling framework. *J. Space Weather Space Clim.*, *11*, 42. https://doi.org/10.1051/swsc/2021020

Gombosi, T. I., Dezeeuw, D. L., Groth, C. P. T., Powell, K. G., Robert Clauer, C., & Song, P. (2001). From Sun to Earth: Multiscale MHD simulations of space weather. In *Space weather* (pp. 169–176). American Geophysical Union (AGU). https://doi.org/10.1029/GM125p0169

Gombosi, T. I., Zeeuw, D. L. D., Powell, K. G., Ridley, A. J., Sokolov, I. V., Stout, Q. F., & Tóth, G. (2003). Adaptive mesh refinement for global magnetohydrodynamic simulation. *Space plasma simulation*, 247–274. https://doi.org/10.1007/3-540-36530-3_12

Gonzalez, W., Joselyn, J.-A., Kamide, Y., Kroehl, H. W., Rostoker, G., Tsurutani, B., & Vasyliunas, V. (1994). What is a geomagnetic storm? *Journal of Geophysical Research*, *99*(A4), 5771–5792. https://doi.org/10.1029/93JA02867

Gosling, J. (1997). Coronal mass ejections: An overview. In *Washington DC American Geophysical Union Geophysical Monograph Series* (Vol. *99*, pp. 9–16). https://doi.org/10.1029/GM099p0009

Gosling, J., Hundhausen, A., & Bame, S. (1976). Solar wind stream evolution at large heliocentric distances: Experimental demonstration and the test of a model. *Journal of Geophysical Research*, *81*(13), 2111–2122. https://doi.org/10.1029/JA081i013p02111

Hundhausen, A. J. (2012). *Coronal expansion and solar wind* (Vol. 5). Springer Science & Business Media. https://doi.org/10.1007/978-3-642-65414-5

Janhunen, P., Palmroth, M., Laitinen, T., Honkonen, I., Juusola, L., Facskó, G., & Pulkkinen, T. I. (2012). The GUMICS-4 global MHD magnetosphere–ionosphere coupling simulation. *Journal of Atmospheric and Solar-Terrestrial Physics*, *80*, 48–59. https://doi.org/10.1016/j.jastp.2012.03.006

Jauer, P. R., Wang, C., Souza, V., Alves, M., Alves, L., Pádua, M., et al. (2019). A global magnetohydrodynamic simulation study of ultra-low-frequency wave activity in the inner magnetosphere: Corotating interaction region+ Alfvénic fluctuations. *The Astrophysical Journal*, *886*(1), 59. https://doi.org/10.3847/1538-4357/ab4db5

Jaynes, A. N., Baker, D. N., Singer, H. J., Rodriguez, J. V., Loto'aniu, T. M., Ali, A. F., et al. (2015). Source and seed populations for relativistic electrons: Their roles in radiation belt changes. *Journal of Geophysical Research A: Space Physics*, *120*(9), 7240–7254. https://doi.org/10.1002/2015JA021234

Johansson, T., Bonnell, J. W., Cully, C., Donovan, E., Raeder, J., Eriksson, S., et al. (2009). Observation of an inner magnetosphere electric field associated with a BBF-like flow and PBIs. *Annales Geophysicae*, *27*(4), 1489–1500. https://doi.org/10.5194/angeo-27-1489-2009

Keesee, A. M., Buzulukova, N., Mouikis, C., & Scime, E. E. (2021). Mesoscale structures in Earth's magnetotail observed using energetic neutral atom imaging. *Geophysical Research Letters*, *48*(3), e2020GL091467. https://doi.org/10.1029/2020GL091467

Kilpua, E., Koskinen, H. E., & Pulkkinen, T. I. (2017). Coronal mass ejections and their sheath regions in interplanetary space. *Living Reviews in Solar Physics*, *14*(1), 1–83. https://doi.org/10.1007/s41116-017-0009-6

Kivelson, M. G., & Russell, C. T. (1995). Introduction to space physics. In *Introduction to Space Physics* (Vol. *586*).

Kletzing, C. A., Kurth, W. S., Acuna, M., MacDowall, R. J., Torbert, R. B., Averkamp, T., et al. (2013). The electric and magnetic field instrument suite and integrated science (EMFISIS) on RBSP. *Space Science Reviews*, *179*(1–4), 127–181. https://doi.org/10.1007/s11214-013-9993-6

Lejosne, S., & Kollmann, P. (2020). Radiation belt radial diffusion at Earth and beyond. *Space Science Reviews*, *216*(1), 19. https://doi.org/10.1007/s11214-020-0642-6

Lemen, J. R., Title, A. M., Akin, D. J., Boerner, P. F., Chou, C., Drake, J. F., et al. (2012). The Atmospheric imaging Assembly (AIA) on the solar dynamics observatory (SDO). *Solar Physics*, *275*(1–2), 17–40. https://doi.org/10.1007/s11207-011-9776-8

Lopez, R. E., Baker, D. N., & Allen, J. (2004). Sun unleashes Halloween storm. *Eos, Transactions American Geophysical Union*, *85*(11), 105–108. https://doi.org/10.1029/2004EO110002

Lyon, J., Fedder, J., & Mobarry, C. (2004). The Lyon–Fedder–Mobarry (LFM) global MHD magnetospheric simulation code. *Journal of Atmospheric and Solar-Terrestrial Physics*, *66*(15–16), 1333–1350. https://doi.org/10.1016/j.jastp.2004.03.020

Mauk, B., Fox, N. J., Kanekal, S., Kessel, R., Sibeck, D., & Ukhorskiy, a. A. (2012). Science objectives and rationale for the radiation belt storm probes mission. In *The Van Allen Probes mission* (pp. 3–27). Springer. https://doi.org/10.1007/978-1-4899-7433-4_2

Mauk, B. H., Fox, N. J., Kanekal, S. G., Kessel, R. L., Sibeck, D. G., & Ukhorskiy, A. (2013). Science objectives and rationale for the radiation belt storm probes mission. *Space Science Reviews*, *179*(1–4), 3–27. https://doi.org/10.1007/s11214-012-9908-y

Miyoshi, Y., Shinohara, I., Takashima, T., Asamura, K., Higashio, N., Mitani, T., et al. (2018). Geospace exploration project ERG. *Earth Planets and Space*, *70*(1), 1–13. https://doi.org/10.1186/s40623-018-0862-0

O'Dwyer, B., Del Zanna, G., Mason, H. E., Weber, M. A., & Tripathi, D. (2010). SDO/AIA response to coronal hole, quiet Sun, active region, and flare plasma. *Astronomy and Astrophysics*, *521*, A21. https://doi.org/10.1051/0004-6361/201014872

Ogino, T., Walker, R. J., & Ashour-Abdalla, M. (1994). A global magnetohydrodynamic simulation of the response of the magnetosphere to a northward turning of the interplanetary magnetic field. *Journal of Geophysical Research*, *99*(A6), 11027–11042. https://doi.org/10.1029/93JA03313

Ozeke, L. G., Mann, I. R., Murphy, K. R., Jonathan Rae, I., & Milling, D. K. (2014). Analytic expressions for ULF wave radiation belt radial diffusion coefficients. *Journal of Geophysical Research: Space Physics*, *119*(3), 1587–1605. https://doi.org/10.1002/2013JA019204

Palmroth, M., Pulkkinen, T., Janhunen, P., & Wu, C.-C. (2003). Stormtime energy transfer in global MHD simulation. *Journal of Geophysical Research*, *108*(A1), 1048. https://doi.org/10.1029/2002JA009446

Paral, J., Hudson, M., Kress, B., Wiltberger, M., Wygant, J., & Singer, H. (2015). Magnetohydrodynamic modeling of three van allen probes storms in 2012 and 2013. In *Annales geophysicae* (Vol. *33*, pp. 1037–1050). https://doi.org/10.5194/angeo-33-1037-2015

Perreault, P., & Akasofu, S. (1978). A study of geomagnetic storms. *Geophysical Journal International*, *54*(3), 547–573. https://doi.org/10.1111/j.1365-246X.1978.tb05494.x

Pollock, C., Moore, T., Jacques, A., Burch, J., Gliese, U., Saito, Y., et al. (2016). Fast plasma investigation for magnetospheric multiscale. *Space Science Reviews*, *199*(1–4), 331–406. https://doi.org/10.1007/s11214-016-0245-4

Powell, K. G., Roe, P. L., Linde, T. J., Gombosi, T. I., & De Zeeuw, D. L. (1999). A solution-adaptive upwind scheme for ideal magnetohydrodynamics. *Journal of Computational Physics*, *154*(2), 284–309. https://doi.org/10.1006/jcph.1999.6299

Pulkkinen, A., Lindahl, S., Viljanen, A., & Pirjola, R. (2005). Geomagnetic storm of 29–31 October 2003: Geomagnetically induced currents and their relation to problems in the Swedish high-voltage power transmission system. *Space Weather*, *3*(8), S08C03. https://doi.org/10.1029/2004SW000123

Raeder, J., Larson, D., Li, W., Kepko, E. L., & Fuller-Rowell, T. (2008). OpenGGCM simulations for the THEMIS mission. *Space Science Reviews*, *141*(1), 535–555. https://doi.org/10.1007/s11214-008-9421-5

Ridley, A., De Zeeuw, D., Manchester, W., & Hansen, K. (2006). The magnetospheric and ionospheric response to a very strong interplanetary shock and coronal mass ejection. *Advances in Space Research*, *38*(2), 263–272. https://doi.org/10.1016/j.asr.2006.06.010

Russell, C. T., Anderson, B. J., Baumjohann, W., Bromund, K. R., Dearborn, D., Fischer, D., et al. (2014). The magnetospheric multiscale magnetometers. *Space Science Reviews*, *199*(1–4), 189–256. https://doi.org/10.1007/s11214-014-0057-3

Schindler, K. (2006). *Physics of space plasma activity*. Cambridge University Press.

Schödel, R., Baumjohann, W., Nakamura, R., Sergeev, V. A., & Mukai, T. (2001). Rapid flux transport in the central plasma sheet. *Journal of Geophysical Research*, *106*(A1), 301–313. https://doi.org/10.1029/2000JA900139

Schwenn, R. (2006). Space weather: The solar perspective. *Living Reviews in Solar Physics*, *3*(1), 1–72. https://doi.org/10.12942/lrsp-2006-2

Shue, J.-H., Song, P., Russell, C., Steinberg, J., Chao, J., Zastenker, G., et al. (1998). Magnetopause location under extreme solar wind conditions. *Journal of Geophysical Research*, *103*(A8), 17691–17700. https://doi.org/10.1029/98JA01103

Siebert, K., & Siscoe, G. (2002). Dynamo circuits for magnetopause reconnection. *Journal of Geophysical Research*, *107*(A7), SMP-6. https://doi.org/10.1029/2001JA000237

Smith, E. J., & Wolfe, J. H. (1976). Observations of interaction regions and corotating shocks between one and five AU: Pioneers 10 and 11. *Geophysical Research Letters*, *3*(3), 137–140. https://doi.org/10.1029/GL003i003p00137

Souza, V. M., Medeiros, C., Koga, D., Alves, L. R., Vieira, L. E., Dal Lago, A., et al. (2018). Classification of magnetospheric particle distributions via neural networks. In *Machine learning techniques for space weather* (pp. 329–353). Elsevier. https://doi.org/10.1016/B978-0-12-811788-0.00013-5

Tanaka, T. (1995). Generation mechanisms for magnetosphere-ionosphere current systems deduced from a three-dimensional MHD simulation of the solar wind-magnetosphere-ionosphere coupling processes. *Journal of Geophysical Research*, *100*(A7), 12057–12074. https://doi.org/10.1029/95JA00419

Tanaka, T. (2007). Magnetosphere–ionosphere convection as a compound system. *Space Science Reviews*, *133*(1–4), 1–72. https://doi.org/10.1007/s11214-007-9168-4

Toffoletto, F., Sazykin, S., Spiro, R., & Wolf, R. (2003). Inner magnetospheric modeling with the rice convection model. *Space Science Reviews*, *107*(1), 175–196. https://doi.org/10.1023/A:1025532008047

Tóth, G., Sokolov, I. V., Gombosi, T. I., Chesney, D. R., Clauer, C. R., De Zeeuw, D. L., et al. (2005). Space weather modeling framework: A new tool for the space science community. *Journal of Geophysical Research*, *110*(A12), A12226. https://doi.org/10.1029/2005JA011126

Tóth, G., Van der Holst, B., Sokolov, I. V., De Zeeuw, D. L., Gombosi, T. I., Fang, F., et al. (2012). Adaptive numerical algorithms in space weather modeling. *Journal of Computational Physics*, *231*(3), 870–903. https://doi.org/10.1016/j.jcp.2011.02.006

Vasyliunas, V. M. (1975). Theoretical models of magnetic field line merging. *Reviews of Geophysics*, *13*(1), 303–336. https://doi.org/10.1029/RG013i001p00303

Wang, C., Guo, X., Peng, Z., Tang, B., Sun, T., Li, W., & Hu, Y. (2013). Magnetohydrodynamics (MHD) numerical simulations on the interaction of the solar wind with the magnetosphere: A review. *Science China Earth Sciences*, *56*(7), 1141–1157. https://doi.org/10.1007/s11430-013-4608-3

Wang, C., Han, J. P., Li, H., Peng, Z., & Richardson, J. D. (2014). Solar wind-magnetosphere energy coupling function fitting: Results from a global MHD simulation. *Journal of Geophysical Research: Space Physics*, *119*(8), 6199–6212. https://doi.org/10.1002/2014JA019834

Wang, C. P., Xing, X., Bortnik, J., & Chu, X. (2020). Inward propagation of flow-generated Pi2 waves from the plasma sheet to the inner magnetosphere. *Journal of Geophysical Research: Space Physics*, *125*(2), e2019JA027581. https://doi.org/10.1029/2019JA027581

Wiltberger, M., Merkin, V., Lyon, J. G., & Ohtani, S. (2015). High-resolution global magnetohydrodynamic simulation of bursty bulk flows. *Journal of Geophysical Research: Space Physics*, *120*(6), 4555–4566. https://doi.org/10.1002/2015JA021080

Wygant, J., Bonnell, J., Goetz, K., Ergun, R., Mozer, F., Bale, S., et al. (2013). The electric field and waves instruments on the radiation belt storm probes mission. In *The Van Allen Probes mission* (pp. 183–220). Springer.

Zhang, B., Sorathia, K. A., Lyon, J. G., Merkin, V. G., Garretson, J. S., & Wiltberger, M. (2019). GAMERA: A three-dimensional finite-volume MHD solver for non-orthogonal curvilinear geometries, *244*(1), 20. https://doi.org/10.3847/1538-4365/ab3a4c

Zhang, L. Q., Baumjohann, W., Khotyaintsev, Y. V., Burch, J. L., Webster, J., Wang, J. Y., et al. (2020). BBF deceleration down-tail of $x < 15$ re from mms observation. *Journal of Geophysical Research: Space Physics*, *125*(2), e2019JA026837. https://doi.org/10.1029/2019JA026837

Zhang, L. Q., Liu, Z. X., Ma, Z. W., Baumjohann, W., Pu, Z. Y., Dunlop, M. W., et al. (2010). X line distribution determined from earthward and tailward convective bursty flows in the central plasma sheet. *Journal of Geophysical Research: Space Physics*, *115*(A6), A06218. https://doi.org/10.1029/2009JA014429

Zong, Q. (2022). Magnetospheric response to solar wind forcing: Ultra-low-frequency wave–particle interaction perspective. In *Annales geophysicae* (Vol. *40*, pp. 121–150). https://doi.org/10.5194/angeo-40-121-2022